2000

A comparison of experimental and computational analyses of two dimensional foil sections.

Fairman, Randall S.

Monterey, California. Naval Postgraduate School

A Comparison of Experimental and Computational Analyses of Two Dimensional Foil Sections

by

Randall S. Fairman

B.S., University of Washington (1991)

Submitted to the Department of Ocean Engineering and Mechanical Engineering
in partial fulfillment of the requirements for the degrees of

Naval Engineer

and

Master of Science in Mechanical Engineering

at the

MASSACHUSETTS INSTITUTE OF TECHNOLOGY

June 2000

A Comparison of Experimental and Computational Analyses of Two Dimensional Foil Sections

by

Randall S. Fairman

Submitted to the Department of Ocean Engineering and Mechanical Engineering
on 13 May 2000, in partial fulfillment of the
requirements for the degrees of
Naval Engineer
and
Master of Science in Mechanical Engineering

Abstract

Performance of two dimensional foil sections with traditional, blunt and cupped trailing edge geometries are experimentally and computationally evaluated. Traditional foils show less than 1% error in lift slope and less than 0.1 degree error in predicted angle of attack. Foils which include trailing edge separation due to a trailing edge cup show up to 30% error in lift slope and 1.0 degree error in predicted angle of attack. Foils which include trailing edge separation due to bluntness show good correlation in lift slop (2% error) but still show up to 0.9 degree error in predicted angle of attack.

Experimental and numerical evaluations are conducted in order to assess whether the differences are caused by the experimental or computational fluid dynamics. All known experimental uncertainties are exhausted without explaining the differences between predicted and measured lift.

Thesis Supervisor: Justin E. Kerwin
Title: Professor of Naval Architecture

Thesis Supervisor: Douglas Hart
Title: Associate Professor of Mechanical Engineering

ACKNOWLEDGMENTS

I would first of all like to thank my father in heaven for the opportunity to serve here for...

Psalm 127:1
Unless the LORD builds the house,
its builders labor in vain.
Unless the LORD watches over the city,
the watchmen stand guard in vain.

I thank my wife Robin and children Lily and Ally for their patience, interest and moral support during my time at MIT.

I thank my country and the U.S. Navy for the financial support and time away from the fleet while learning at MIT.

I thank Professor Kerwin for his guidance and interest. He has truly been a consistent example of patience and humility. It is a pleasure to work for a true expert who always listens as if I were the expert. His guidance is responsible for any accurate direction taken in this research. I hope to learn to follow his example in dealing with those that work for me.

So much of what I have done in this thesis has relied on the expertise of others. Specifically, Rich Kimball is responsible for the success of the laser doppler velocimetry measurements. Alexandra Techet is responsible for all of the particle image velocimetry measurements and evaluation. Mike Griffin is responsible for the analyses accomplished in IFLOW.

The support for this research was provided in part under the Office of Naval Research grant #N00014-95-1-0389, Dr. Edwin Rood, Program Manager.

Contents

List of Figures

List of Tables

Chapter 1

Introduction

1.1 Motivation

Military and civilian ships are demanding higher speeds and improved cavitation performance. These requirements are pushing current propulsion system designers to rapidly improve existing systems. One of the directions these advancements are pushing designers is toward novel new section designs in propeller blades.

Based upon analyses accomplished to date, it is not clear computational fluid dynamics codes are accurate for the advanced section designs considered. The following is the abstract from a thesis conducted by Jorgen Jorde [1] in December 1995:

> "This thesis covers a comparison between experimental and numerical results of a foil with a slightly cupped trailing edge, and a foil with a more distinctly cupped trailing edge.
>
> Experiments have been conducted to find lift and drag coefficients, as well as boundary layer parameters at the trailing edges of both foils. The experiments indicate that the numerical tools available are not capable of accurately predicting the lift of these foils.
>
> Analysis of the results further indicate that experiments where there is a great wall/foil interaction are difficult to interpret until numerical tools are refined to the extent that they may be the link to the performance in unbounded flow."

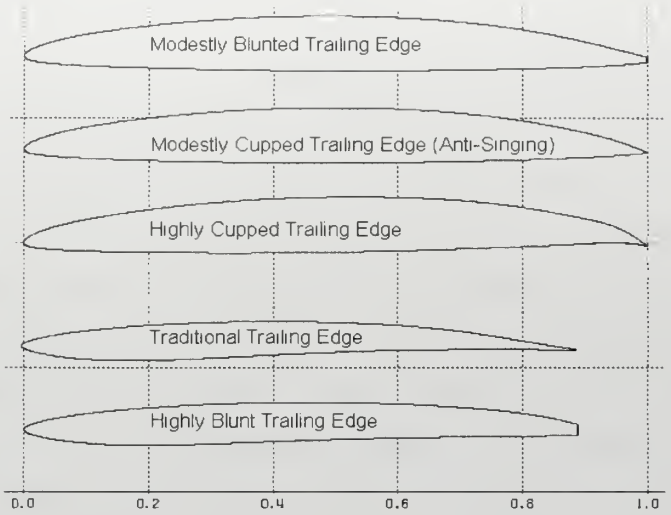

Figure 1-1: Range of Foil Geometries Considered

The numerical tools have now been refined to the extent that they can analyze the behavior of multiple foil elements and simulate the effects of the tunnel walls. The present thesis attempts to answer the questions raised by Jorde by applying the advancements in numerical tools over the last five years and improving upon the experimental techniques and analysis.

1.2 Goal

The goal of this thesis is to assess the capabilities of experimentation and computational fluid dynamics in predicting performance of challenging foil section designs.

1.3 Method

This thesis initially focuses on a single foil, at a single angle of attack, at a single Reynolds Number and seeks to assess whether there is agreement between experimental and computational analyses of this foil under this specific set of conditions. The foil with the highly cupped trailing edge shown in Figure 1-1 is the initial area of focus and is the same foil used by Jorde [1] analyzed in 1995. Questions that arise from the analysis of this foil drives the thesis toward a wider consideration of the foil geometries depicted in Figure 1-1.

1.3.1 Cupped Foil Experimental Analysis

This section improves upon existing experimental methods and applies them to establish a confidence interval for the performance of the foil being assessed. The initial assessment of the experimental methods available call into question the ability to accurately measure fluid dynamic drag. Methods are developed for determining pressure in the wake which allows refinement of traditional methods as well as a new thermodynamic analysis to determine drag. The methods for calculating drag are applied to a control case of a two dimensional cylinder to assess their performance. These methods are then applied to this foil to establish a confidence interval for fluid dynamic drag. The initial assessment of the experimental methods for calculating lift seem to indicate that existing methods are acceptable. An extensive data field is taken to allow a convergence study, error analysis and confidence interval for the fluid dynamic lift.

1.3.2 Cupped Foil Numerical Analysis

This section applies the most recent updates of numerical procedures to establish a confidence interval for the performance of the same foil in computational fluid dynamics. This section shows good agreement between computational fluid dynamics methods, but the predicted lift slope is 30% larger than the measured lift slope and there is a one degree offset in angle of attack. This discrepancy between experiment and computation is so large that it brings into question the experimental results as well as the computational results.

1.3.3 Analysis of Numerical and Experimental Solution Incompatibility

This section of the thesis seeks to explain why the experiment and predictions are so far out of agreement on this foil. Several avenues that did not bear fruit in explaining the differences are discussed. At the conclusion of the analyses on the very difficult highly cupped foil both the experiment and computations appear valid, but still show very different answers.

1.3.4 Analysis of Other Foil Sections

This section of the thesis then seeks to see whether the performance of other foils in our water tunnel can be predicted. The five foil geometries shown in Figure 1-1 are evaluated. In this section it is shown that there is very good agreement between the computational and experimental fluid dynamics for the case where the foil takes the traditional approach of unloading the foil over the last 10% of the chord length and ending at a sharp point. It is shown that when the foil ends at a blunt trailing edge or when it is not unloaded at the trailing edge agreement is not achieved.

1.3.5 Conclusions

In the conclusions the assertion is made that CFD performs well for foils that are unloaded near the trailing edge, but shows significant errors when separation occurs under asymmetric loading. Some speculative reasons for these inaccuracies are proposed.

Chapter 2

Cupped Foil Experimental Analysis

The experimental analysis conducted by Jorgen Jorde [1] is extensive. He conducted a significant evaluation of the gross flow field velocities and boundary layer measurements. The experimentation and analysis conducted here seeks to extend and improve upon his efforts to allow more accurate determination of drag coefficient as well as error analysis for both lift and drag.

2.1 Experimental Overview

The MIT Variable Pressure Water Tunnel (Figure 2-1) is a closed loop system. A variable speed impeller forces flow through the loop at speeds up to 9 m/sec.

The test section is twenty inches square and features removable clear windows on all four sides. In the test section, a three watt argon-ion laser doppler velocimeter is used to measure local vertical and horizontal velocities. The laser measurement volume is less than 0.07 mm across and 0.7 mm deep. Mean velocities are repeatable to within 0.002 m/sec with the sample sizes taken in this experiment. Velocities are accurate to within 0.6%. A Kiel Probe is used to measure differential stagnation pressure from the front of the foil to the wake. The measurement diameter for the Kiel Probe is approximately 2 mm.

Figure 2-2 is a depiction of all data taken in the initial phase of this experiment. The chord length of the foil is 455 mm. Fluid velocities are taken at a path length interval of 3 mm along all of the lines except for the vertical lines in the wake of the foil. The vertical lines in

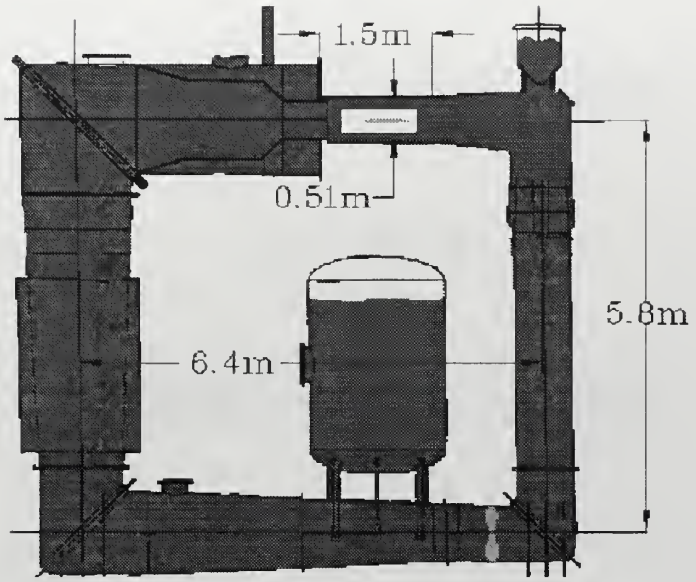

Figure 2-1: MIT Variable Pressure Water Tunnel

the wake of the foil are actually 5 vertical lines of data taken at a 1 mm spacing which allow for calculating flow gradients in the longitudinal direction. The foil angle of attack is fixed at 0.35±0.05 degrees. The horizontal tunnel velocity is maintained constant throughout the experiment at 7.003 m/sec. The velocity is held constant to within 0.3% and is accurate to within 0.6%.

2.2 Pressure Measurement

The pressure throughout the majority of the fluid domain is determined based on Bernouli's Equation [2]. In the wake there has been significant fluid flow energy converted to internal energy such that Bernouli's Equation is not valid. In this region two methods of pressure measurement are used in this experiment. The first method, already discussed is the Kiel Probe. The second method is to apply measured velocity gradients to the Navier Stokes Equations and calculate the pressure variation.

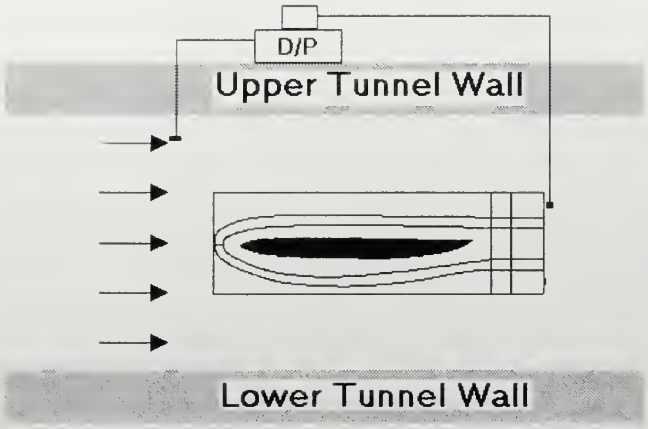

Figure 2-2: Test Section Layout and Data Summary

2.2.1 Derivation

Beginning with the vertical component of the Navier Stokes Equation,

$$\underbrace{u\frac{dv}{dx} + v\frac{dv}{dy} + w\frac{dv}{dz} = -\frac{1}{\rho}\frac{dp}{dy} + \mu\nabla^2 v}_{\text{Navier Stokes Equation}} \tag{2.1}$$

where

u = fluid velocity in x direction

v = fluid velocity in y direction

w = fluid velocity in z direction

p = static pressure

ρ = fluid density

μ = fluid viscosity

The flow domain considered for this application is approximated as two dimensional so the $w\frac{dv}{dz}$ term is negligible. The low viscosity of the fluid integrated over this small length causes the viscous ($\mu\nabla^2 v$) term to also be negligible. Each of the velocities is considered with a mean

and fluctuating component which yields Equation 2.1 from Equation 2.2.

$$-\frac{1}{\rho}\frac{dp}{dy} = \bar{u}\frac{d\bar{v}}{dx} + \bar{v}\frac{d\bar{v}}{dy} + \acute{u}\frac{d\acute{v}}{dx} + \acute{v}\frac{d\acute{v}}{dy} \tag{2.2}$$

where

$$\begin{aligned} \bar{u} &= \text{mean x direction velocity} \\ \bar{v} &= \text{mean y direction velocity} \\ \acute{u} &= \text{fluctuating x direction velocity} \\ \acute{v} &= \text{fluctuating y direction velocity} \end{aligned}$$

The fluid velocity gradients in the x direction are determined using a least squares fit from five points at an interval to give best gradient resolution. In order to transform this equation into a form reliant on horizontal gradients and into a form reliant on physically measured quantities, a few substitutions are made. Equation 2.3 is simply the continuity equation in two dimensions.

$$0 = \frac{du}{dx} + \frac{dv}{dy} \tag{2.3}$$

Equation 2.4 is simply an identity for the derivative of a product.

$$\acute{u}\frac{d\acute{v}}{dx} = \frac{d}{dx}\acute{u}\acute{v} - \acute{v}\frac{d\acute{u}}{dx} \tag{2.4}$$

Applying these equations and taking the time average gives Equation 2.5 which is the form that is directly applied to the measured data.

$$-\frac{1}{\rho}\frac{d\bar{p}}{dy} = \bar{u}\frac{d\bar{v}}{dx} + \bar{v}\frac{d\bar{u}}{dx} + \frac{d}{dx}\overline{\acute{u}\acute{v}} + \frac{d}{dy}\overline{\acute{v}^2} \tag{2.5}$$

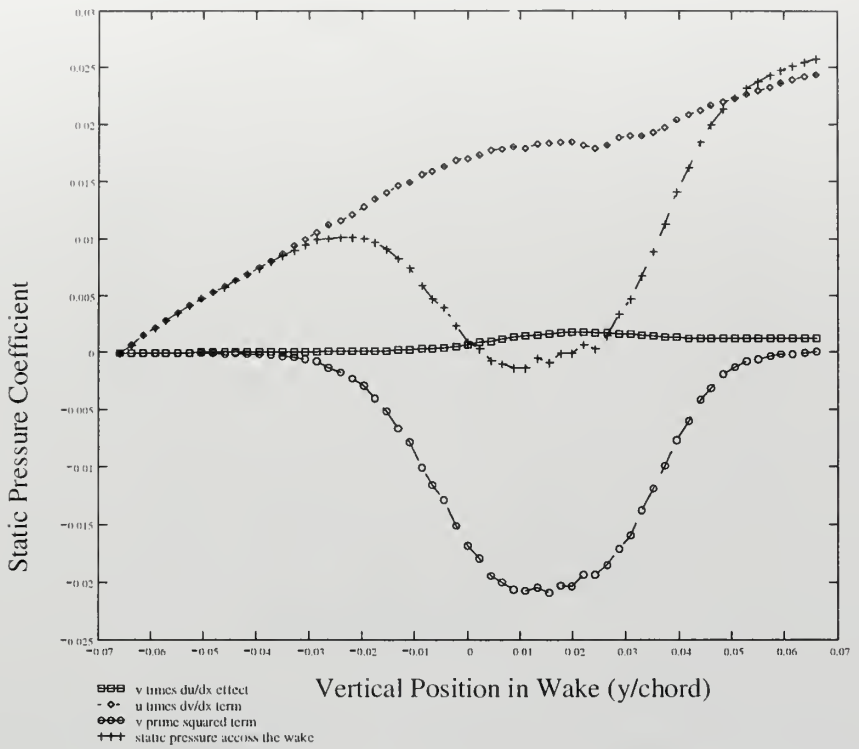

Figure 2-3: Pressure Variation by Component

The laser doppler velocimeter used in this experiment simultaneously samples the velocity of a particle in the horizontal and vertical directions. This feature allows a statistical analysis of $\overline{\acute{u}\acute{v}}$ and $\overline{\acute{v}^2}$ at each point in space.

2.2.2 Results

Appendix B shows the raw data taken in this experiment. The $\frac{d}{dx}\overline{\acute{u}\acute{v}}$ term is found to be two orders of magnitude smaller than the other components. The effect of the other individual terms shown in Equation 2.5 on pressure is plotted in Figure 2-3. The $\bar{v}\frac{d\bar{u}}{dx}$ has very little impact on the overall problem which could have been anticipated by the fact that both $\bar{v}$ and $\frac{d\bar{u}}{dx}$ are small quantities. The $\bar{u}\frac{d\bar{v}}{dx}$ term provides the appropriate slope for the two sides of the boundary layer to return to the expected Bernouli Pressure. The $\frac{d}{dy}\overline{\acute{v}^2}$ term gives the pressure dent in the center of the wake that is caused by the turbulent viscous effects.

Figure 2-4 shows the results of plotting stagnation pressure measured with a Kiel Probe

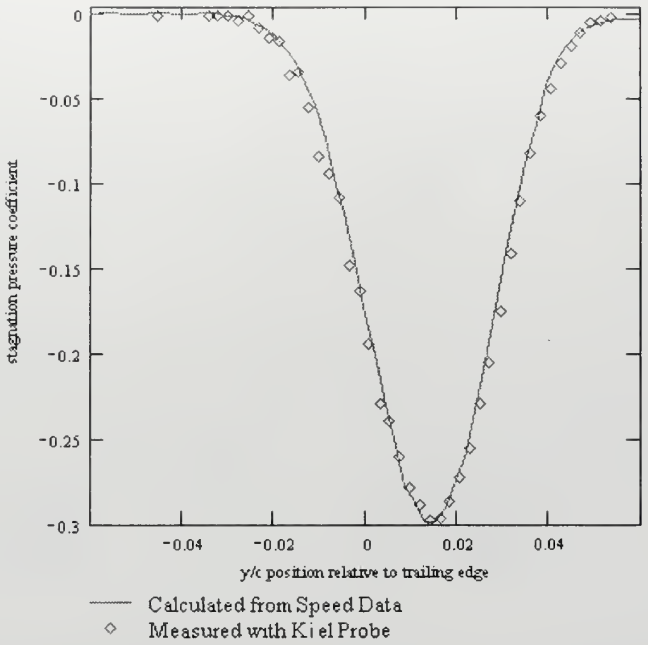

Figure 2-4: Stagnation Pressure Coefficient vs Vertical Wake Position

and stagnation pressure inferred from the Navier Stokes Equations as shown above.

As a brief comment to experimentalists, obtaining accurate flow gradients in the wake region is not a trivial matter. In order to obtain sufficiently repeatable vertical velocities to accurately distinguish gradient information it was necessary to take 3000 velocity samples at each point in space. On top of this, it was necessary to take five separate sample points at an appropriate spacing in the horizontal direction to obtain the slope using a least squares fit. In short, this means 15,000 velocity samples to obtain flow gradients at a single point in space. The gradients through the wake need to be resolved at a maximum spacing of 1 mm. With a wake thickness of about 40 mm this translates to 600,000 velocity samples to obtain the pressure information across the wake at one location. Figure 2-5 shows the pressure determined from velocity magnitudes and gradients at three longitudinal positions in the wake.

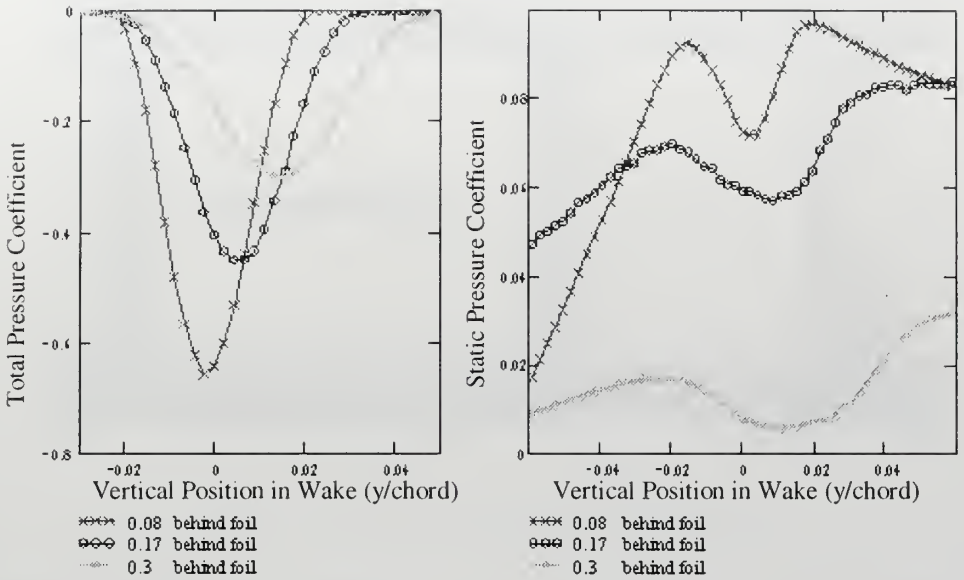

Figure 2-5: Stagnation and Static Pressure in the Foil Wake at Three Longitudinal Positions

2.3 Drag Measurement

2.3.1 Overview

Experimental measurement of profile drag is given considerable attention in wind tunnel testing and water tunnel testing. Measurement of profile drag requires knowledge of pressure and velocity. Until recently, velocity was inferred from pressure measurements because direct measurement of fluid velocity was not available. Schlichting [2] summarizes various methods of calculating drag on a foil based strictly on pressure measurements in the wake of the foil. These methods have been demonstrated to be accurate when taking measurements in the wake of the foil at least 0.05 chord length behind the foil. A potential weakness of these methods explored in this thesis is inaccuracy dealing with unsteadiness in a wake.

In recent years laser doppler anemometry has given experimentalists the ability to directly measure velocity in a fluid domain. This capability provides great insight into the nature of the flow in the wake and allows accurate measurements of fluid velocity and turbulence intensity. Kinnas [3] developed a method for inferring fluid dynamic drag based solely on velocity information. This method assumes the pressure across the wake can be determined

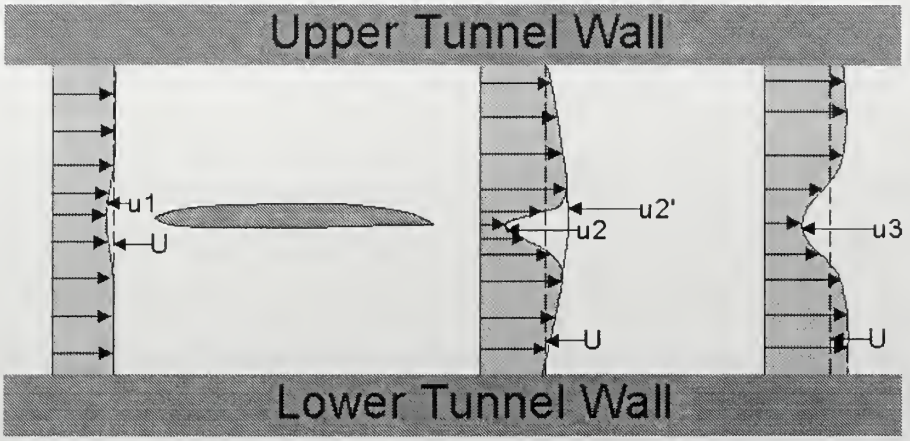

Figure 2-6: Velocity Definitions for Analyses

by linear interpolation from one edge to the other. The difference in static pressure between the method of Kinnas and the measured values shown in Figure 2-5 equates to an 8% error in drag measurement. The bigger problem with this method for this particular application is the effect of sidewall boundary layer growth on the overall measurement. Appendix A summarizes the effect of sidewall boundary layer growth on a control volume analysis for drag. It has been the conclusion of Kimball [4], Jorde [1] and this study that the bounding box method is not well suited to water tunnel testing.

This study adds to these methods another based on thermodynamics. The theory is covered and then a very challenging unsteady problem of measuring drag on a cylinder is tested. The thermodynamic method provides results within 2.5% of the direct measurement of the cylinder drag while all of the other methods are 13% or more in error. Three methods are then applied to the foil of interest and the average value of each method is found to agree within 1% of the other methods. The reason the methods agree well in the case of the foil, but not in the case of the cylinder is that only the thermodynamic method takes into account unsteadiness in the wake. The cylinder has significant unsteadiness in the wake and the foil has relatively little.

2.3.2 Experimental Drag Measurement Theory

Momentum Methods

Equation 2.6 can be used to determine fluid dynamic drag on the foil if the fluid velocities and pressures are known all the way around a closed contour that surrounds the body. One example of such a contour is the flow domain that stretches from the top to the bottom of the tunnel in front and in back of the foil. This control volume is the one used in the method of Betz and the method of Jones, which are summarized by Schlichting [2]. Another possibility would be to simply measure the fluid velocity all the way around the foil, and this control volume is the one used in the method of Kinnas [3].

Momentum Contour Integration (Kinnas)

$$D = -\rho \oint \left[uvdx + \left(u^2 + u_{rms}^2\right) dy\right] + \oint p dy \tag{2.6}$$

u=horizontal velocity

v=vertical velocity

p=static pressure

Analyzing the control volume that stretches from the top to the bottom of the tunnel is complicated by the fact that velocities are not known all the way to the edge of the tunnel. In order to analyze this control volume it is necessary to transform Equation 2.6 into a differential form that tends to zero outside of the wake. In Betz formulation, a false source is used to raise the fluid velocity u2 to u2' to provide a useful flow field with a constant stagnation pressure. He then uses the drag associated with the false source as a correction to the change in total pressure portion of the formulation. Equation 2.7 is used to calculate fluid dynamic drag based on the method of Betz.

Betz' Formulation

$$D = \int_{-\infty}^{\infty} [g_1 - g_2]\, dy + \frac{\rho}{2} \int_{-\infty}^{\infty} \left[(u_2 - u_2')\left(u_2' + u_2 - 2U_\infty\right)\right] dy \tag{2.7}$$

$$g = p + \frac{\rho u^2}{2}$$

U_∞=free stream velocity

Jones formulation assumes the fluid will travel from 2 to 3 with no further losses. Point 3

is sufficiently far downstream to allow the static pressure to equalize across the wake. He uses continuity along a streamtube to project conditions at 2 back to point 3 where the static pressure has returned to free stream conditions and is no longer contributing to drag. He then simply evaluates the momentum deficit at point 3. Equation 2.8 is used to calculate fluid dynamic drag based on the method of Jones.

$$D = \int_{-\infty}^{\infty} [u_2 (U_\infty - u_3)] \, dy \qquad \text{Jones' Formulation} \tag{2.8}$$

Thermodynamic Method

The first law of thermodynamics states that the rate at which work is done on a control volume is equal to the net energy flux out of the control volume. Consider the control volume between 1 and 2 in Figure 2-6. The force on the foil is stationary relative to a fixed coordinate system; therefore, no net work is done on the control volume. Based on the first law of thermodynamics there can be no net change in fluid energy from 1 to 2. There is a reduction in flow energy and kinetic energy that is being converted to fluid internal energy. This process is irreversible. Equation 2.9 shows the change in fluid internal energy from 1 to 2.

$$E_2 = \left(\frac{\rho}{2} U_\infty^2 + p_\infty\right) - \left(\frac{\rho}{2} U_2^2 + p_2\right) + E_\infty = g_\infty - g_2 + E_\infty \tag{2.9}$$

$$E = \text{Fluid Internal Energy} \tag{2.10}$$

In order to evaluate the system using the second law of thermodynamics it is desired to project the change in internal energy to 3. Jones' method was to assume no further losses, but with flow separation unsteadiness in the wake must also be considered. It is assumed that the energy associated with the unsteadiness in the wake will be converted to internal energy via viscous dissipation. Calculation of energy associated with the unsteadiness is taken from Schlichting [2]. The fluid internal energy at 3 is then given by Equation 2.11.

$$E_3 = g_\infty - g_2 - \frac{\rho}{2} \left(u_{rms_2}^2 + v_{rms_2}^2\right) + E_\infty \tag{2.11}$$

Equation 2.12 is the basic relation for calculating a change in fluid entropy based on a change in fluid internal energy. It is a direct result of the second law of thermodynamics [5].

$$\begin{aligned} TdS &= dE + Pdv \\ P &= pressure \\ v &= \text{change in volume} \\ S &= entropy \end{aligned} \tag{2.12}$$

Water is incrompressible so there is no change in volume so Equation 2.12 reduces to 2.13.

$$S_3 - S_\infty = \frac{E_3 - E_\infty}{T_0} \tag{2.13}$$

The "lost work rate" associated with this entropy generation is given by Equation 2.14.

$$\mathring{\mathrm{W}}_{lost} = \int \left[T_0 \left(S_3 - S_\infty\right) u\right] dy \tag{2.14}$$

The drag on the hydrofoil based on this analysis is given by Equation 2.15.

$$D = \frac{\mathring{\mathrm{W}}_{lost}}{U} \tag{2.15}$$

2.3.3 Results

In order to assess the quality of the various methods in measuring fluid dynamic drag in an unsteady wake a cylinder is evaluated as a test case. The actual drag on the cylinder is determined by measuring the pressure on the surface of the cylinder through a very small hole and rotating the cylinder. This method of drag measurement assumes small tangential viscous forces on the cylinder surface. The static pressure is integrated around the cylinder to obtain the drag force. The experimental method and results are recorded by Prieto [6]. The direct measurement and each of the other method solutions are summarized in Table 2.1. Each of

the methods show significant error with the exception of the Thermodynamic method which is within 2.5% of the direct measurement.

Technique	Drag Coefficient
Direct Measurement with Pressure Integration	0.77
Betz	0.67
Jones	0.67
Kinnas	0.49
Thermodynamic	0.75

Table 2.1: Summary of Method Results for Cylinder Drag Coefficient

The fluid dynamic drag is also measured for the foil. The drag is calculated at 3 different longitudinal positions; the results are shown in Figure 2-7. The method of Kinnas, Betz and Jones were all applied using the calculated pressure discussed above and the measured velocities. As discussed in Appendix A the method of Kinnas diverges as the control volume size increases due to three dimensional effects. This accounts for the significant deviation between this method of measuring drag and the other three. The methods of Betz and Jones both use the assumption of convection without further losses; therefore, it makes sense that their results would agree. The thermodynamic method provides results very similar to the methods of Betz and Jones. A simple average for each of the three valid methods shows remarkably consistent results as shown in Table 2.2. The conclusion is that the drag coefficient for this foil is 0.0097 with an error margin of 2.5% to encompass all experimental results and stay consistent with the errors measured in the cylinder experiment.

Technique	Drag Coefficient
Betz	0.00969
Jones	0.00973
Thermodynamic	0.00973

Table 2.2: Summary of Method Results for Foil Drag Coefficient

2.4 Lift

Equation 2.16 is derived in many textbooks such as Newman [7].

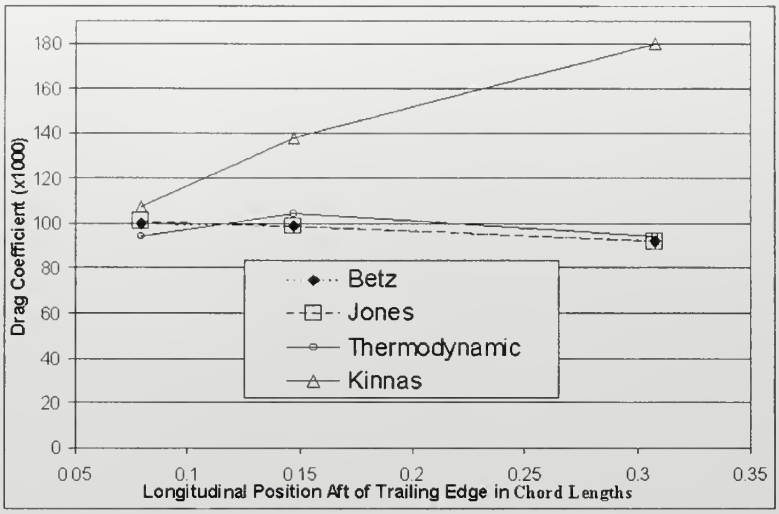

Figure 2-7: Summary of Drag Calculation Methods for the Cupped Foil

Momentum Contour Integration

$$L = -\rho \oint \left[uvdy + \left(v^2 + v_{rms}^2\right) dx\right] + \oint pdx$$

u=horizontal velocity

v=vertical velocity

p=static pressure (2.16)

Figure 2-8 shows the foil in the tunnel with the various control volumes analyzed for lift coefficient by applying Equation 2.16. Appendix B summarizes the data taken along these contours. Based on these results the lift coefficient is determined to be 0.462±0.01.

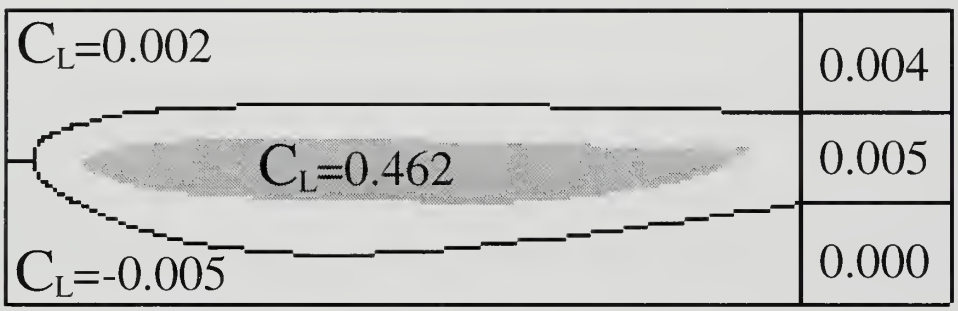

Figure 2-8: Summary of Results for Measured Lift Coefficient

Chapter 3

Numerical Predictions of Cupped Foil Performance

Two computational fluid dynamics codes are used to evaluate the performance of the cupped trailing edge hydrofoil for which experimental evaluation has been conducted at the MIT variable pressure water tunnel. Both codes used model both the foil and the tunnel wall in two dimensions. The two flow codes utilized are IFLOW [8] and MSES [9].

3.1 IFLOW

IFLOW is a Reynolds Averaged Navier Stokes code developed by Sung [8]. IFLOW is capable of solving the two and three-dimensional incompressible steady and unsteady RANS equations and uses a non-linear k - ω turbulence model for closure. The turbulence model is the standard k - ω model developed by Wilcox [10] coupled with a nonlinear Reynolds stress model.

The cupped foil is analyzed in an infinite fluid domain and also with the tunnel walls. The foil performance is verified to be converged by iteration steps and mesh density. Table 3.1 shows the results of this analysis.

Boundary Condition	Lift Coefficient	Drag Coefficient
Infinite Fluid	0.525	0.011
With Viscous Tunnel Walls	0.625	0.012

Table 3.1: Iflow Numerical Results for Cupped Foil

3.2 MSES

MSES uses a boundary layer model to predict boundary layer growth and separation along the foil. The inviscid Euler formulation and integral viscous formulation are coupled through the displacement thickness and solved simultaneously with a global Newton method. The code is developed and adapted for use with blunt trailing edges by Mark Drela [9]. Three methods of analysis are used in MSES.

1. Foil performance is measured in an infinite fluid domain.

2. A built in feature for wind tunnel testing is used to provide the effect of inviscid tunnel walls on the flow regime.

3. The ability to analyze multiple airfoil elements is utilized to put a long thin plate above and below the foil being analyzed. This long thin plate develops a boundary layer similar to the tunnel walls and therefore provides a more accurate depiction of the actual experimental setup. The results determined using this method are 5% lower than the results without top and bottom boundary layers. All results in the following sections are reported based on analyses using this method.

Boundary Condition	Lift Coefficient	Drag Coefficient
Infinite Fluid	0.545	0.009
With Inviscid Tunnel Walls	0.623	0.010
With Viscous Tunnel Walls	0.590	0.010

Table 3.2: Mses Numerical Results for Cupped Foil

3.3 Conclusions

The computational analyses conducted here are about 6% different from one another and about and about 30% off of the experimental measurements. This represents an angle of attack offset (assuming experimental lift slope) of about 0.2 degrees between the two codes and about 1 degree between the experiment and the codes. The results are outside the margin of error in the experiment. The question at hand is whether the margins of error in the experiment

have not been appropriately considered or whether the computational fluid dynamics codes are inaccurate.

Chapter 4

Analysis of Numerical and Experimental Solution Incompatibility

The cupped foil geometry shows consistently poor correlation between experiment and computations over a wide range of angle of attack and Reynolds Number. Figure 4-1 is a summary of the lift measurements taken on this foil. As shown in the diagram, both the computational and numerical calculations have been performed by a range of a people, over a significant period of time, using different equipment and different algorithms, but the end result is a consistent lift prediction that exceeds measured lift prediction by 0.1 to 0.2 depending on angle of attack.

This chapter poses a series of questions that have been addressed in an attempt to reconcile the differences between computational fluid dynamics results and experimental results. Each section includes the parameter or concept in question as well as how this question has been addressed. Several of the sections refer to particle image velocimetry data that was taken to augment the laser doppler velocimetry data. Appendix C covers the experimental procedures and data collected via particle image velocimetry for this experiment.

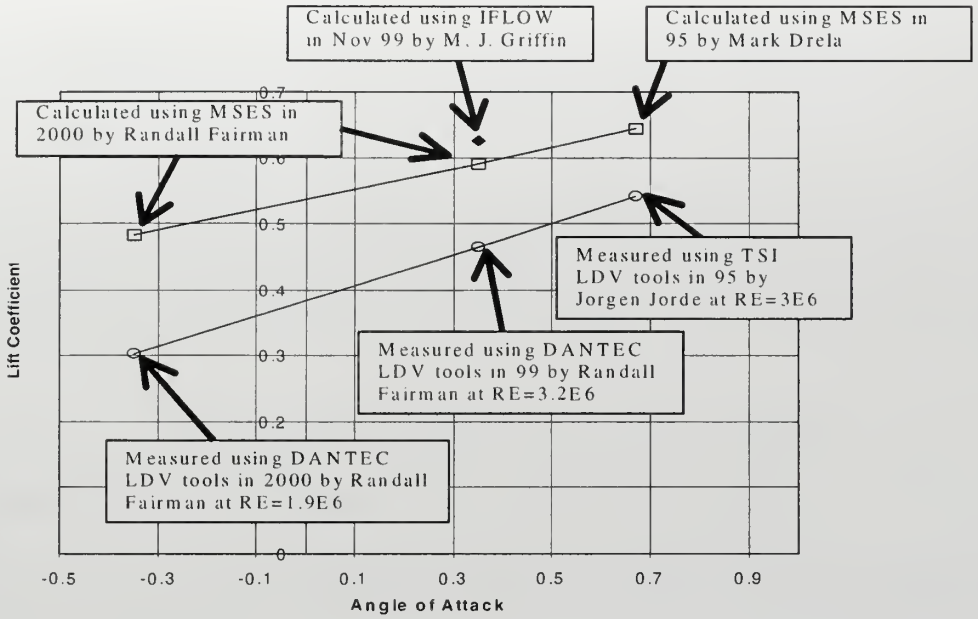

Figure 4-1: Lift Coefficient vs Angle of Attack for Cupped Foil

4.1 Angle of Attack

The first question that naturally arises is whether or not the same angle of attack is being used in the flow codes and in the experiment. Four independent methods of measuring the angle of attack are used.

1. The vertical position of the leading and trailing edges are located using the horizontal beam of the laser doppler velocimeter.

2. The position of various points on the surface of the foil are measured with the laser and these points are fitted to the foil offsets rotated at a specific angle of attack. This method allowed an error analysis of the foil angle of attack by rotating beyond the fit to the point where it is clear that there is no longer agreement. Figure 4-2 shows the foil at 0.35 degrees along with the offsets measured. It was found that if the foil was rotated to 0.3 or 0.4 degrees it is clear that the offsets no longer agree. Based on the second method the foil angle of attack is determined to be 0.35 ± 0.05.

3. A mechanical pointer is connected to a traverse to measure the position of the leading

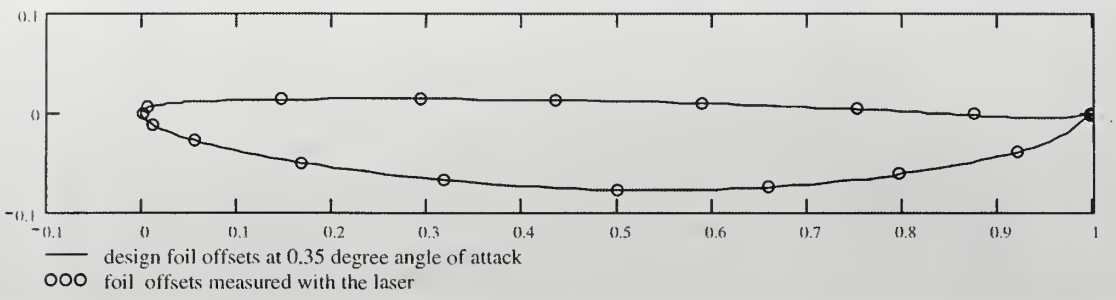

Figure 4-2: Laser Varification of Foil Angle of Attack

and trailing edges of the foil relative to the tunnel horizontal axis.

4. Particle image velocimetry pictures are combined to show the position of the surface of the foil along its length.

In summary, the angle of attack is confident within 0.05 degrees. From Figure 4-1 it is clear that the error in angle of attack is insufficient to be a significant contributor to the discrepancy between experimental and computational results.

4.2 Foil Geometry

The next question that naturally arises is whether or not the foil being modeled in the computational fluid dynamics codes is the same foil analyzed in the experiment. The foil geometry is verified as follows:

1. The foil offsets from the computational fluid dynamics codes are scaled to the experimental foil size.

2. A computer controlled waterjet cutter is used to cut out the foil shape in aluminum.

3. The foil shape is slipped over the foil and inspected for gaps at the edges

The conclusion of this process is that the actual foil shape and evaluated foil shapes are the same.

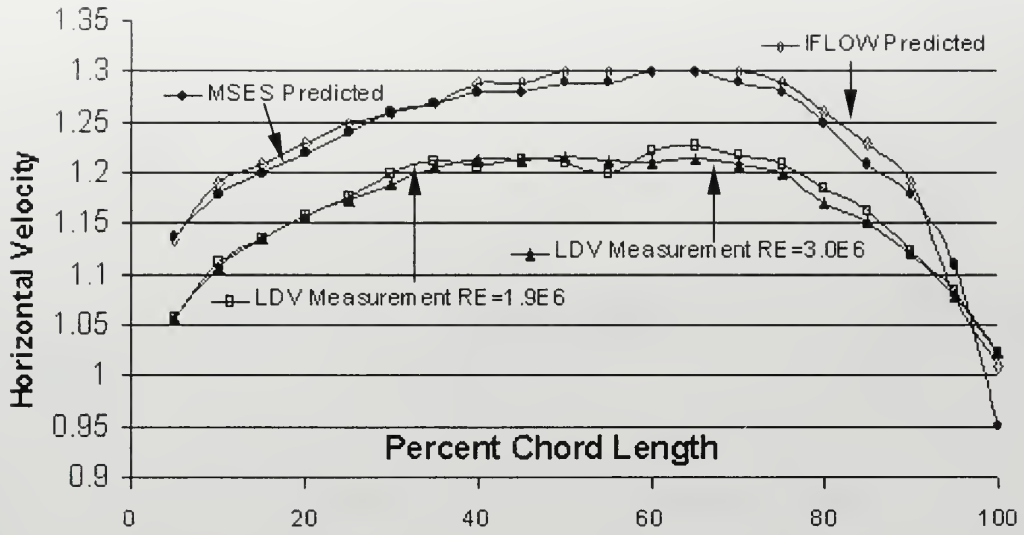

Figure 4-3: Predicted Verses Measured Edge Velocity

4.3 Data Processing Errors

Another issue to consider is whether or not the lift coefficient for the experiment is calculated accurately. This concern is alleviated in three ways.

1. The flow velocity information from IFLOW is used to set up a mock experiment. The fluid velocity at all of the points measured in the experiment are extracted and used to calculate lift using the momentum integration method used in the experiment. The result is that the mock experiment agrees with the IFLOW lift output to the third significant digit. This shows that in the case of perfect data our algorithm performs well within our predicted error margin.

2. Figure 4-3 shows the edge velocities on the suction side of the foil verses chord position. Both the computational and experimental velocities are normalized by velocity measured upstream at a geometrically identical location. It is clear that both computational fluid dynamics codes are predicting a much higher edge velocity than is measured. This higher edge velocity on the suction side of the foil produces a lower pressure and therefore higher lift force.

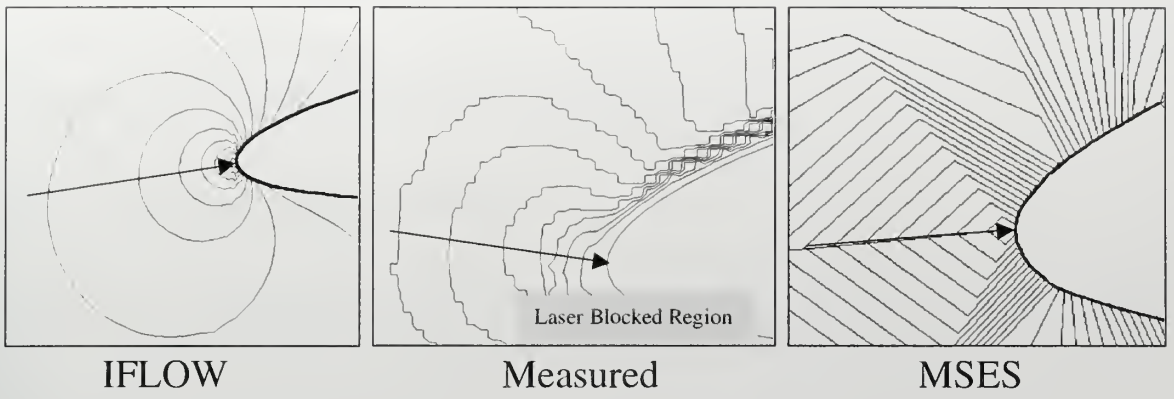

Figure 4-4: Predicted Verses Measured Stagnation Point

3. Figure 4-4 shows the leading edge pressure distribution predicted by IFLOW and MSES as well as the experimentally measured leading edge data. It is clear from this figure that the observed stagnation point is more on the suction side of the foil than the predicted stagnation point. This conclusion is consistent with the fact that the experimentally measured lift is lower than predicted.

4. Figure 4-5 shows the leading edge pressure distribution predicted by MSES when the angle of attack is adjusted to force the lift coefficient to agree with measurements. The updated stagnation point matches closely with the measured stagnation point as is expected. The angle of attack adjustment required to cause this change in lift is -1. degree.

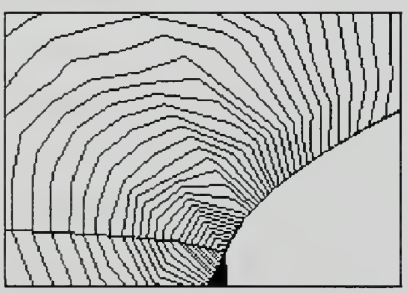

Figure 4-5: MSES Stagnation Point when C_L is Matched with Experimental Results

In summary, it is virtually certain that there are significant differences between predicted and measured flow velocities. The differences in lift are not a function of the method used to measure lift, but an actual difference in the flow field.

4.4 Two Dimensional Flow

Another potential difference between the flow codes and the experiment is a difference in aspect ratio. The computational fluid dynamic codes analyze a two-dimensional solution which uses an infinite aspect ratio assumption. The experiment uses actual foil aspect ratio of 0.9 and uses the tunnel walls to simulate an infinite aspect ratio. These sidewalls actually experience some boundary layer growth and therefore could lead to three dimensional effects in the tunnel.

4.4.1 Gross Flow Field

Jorde [1] measured the flow velocities across the tunnel and showed the flow at a given location in the gross flow field is two dimensional.

4.4.2 Foil Boundary Layers

Although the gross flow field is shown to be two dimensional, it is possible that there are three dimensional effects in the boundary layers which cause changes in boundary layer growth on the foil. These effects could result in significantly different lift, particularly considering that there is a separated flow region near the trailing edge of the foil. In order to eliminate the interaction between the tunnel wall boundary layers and the foil boundary layers fences are constructed out of $\frac{1}{8}$" aluminum and put on the foil to block any travel of the wall boundary layer down the span of the foil. This fence geometry is shown in Figure 4-6. When the actual wake velocities were measured with and without the fences there was no change.

It is possible that the fences used here developed a boundary layer of their own, and then the fence boundary layers interacted with the foil boundary layers to cause a similar effect as the tunnel wall boundary layers. In order to test this hypothesis a set of modified fences were constructed that covered only the last 10% of the foil where there is significant thickness to the boundary layer. This also covers the region where separation is expected. Again the wake

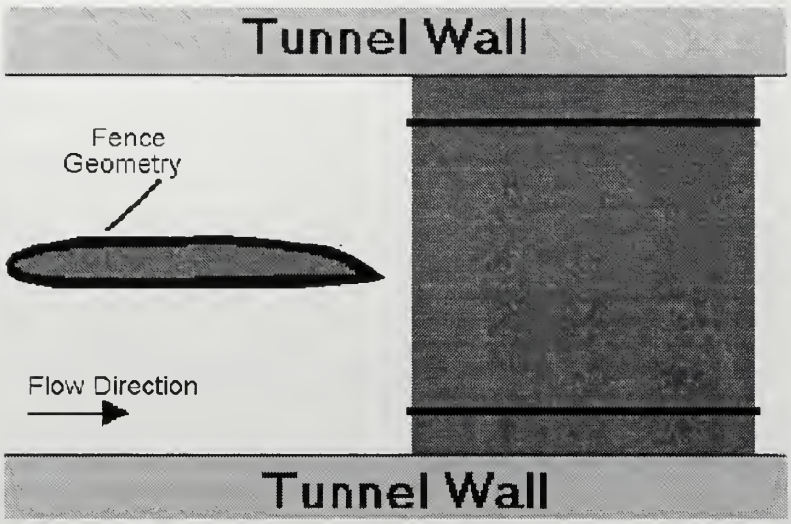

Figure 4-6: Fence Geometry Used to Evaluate Sidewall Boundary Layer Effects

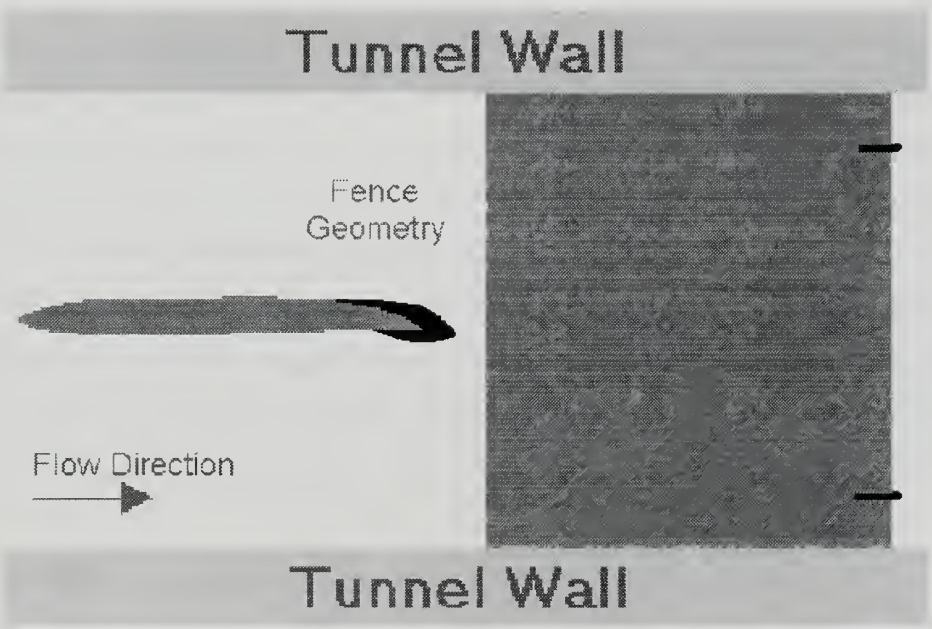

Figure 4-7: Modified Fence Geometry

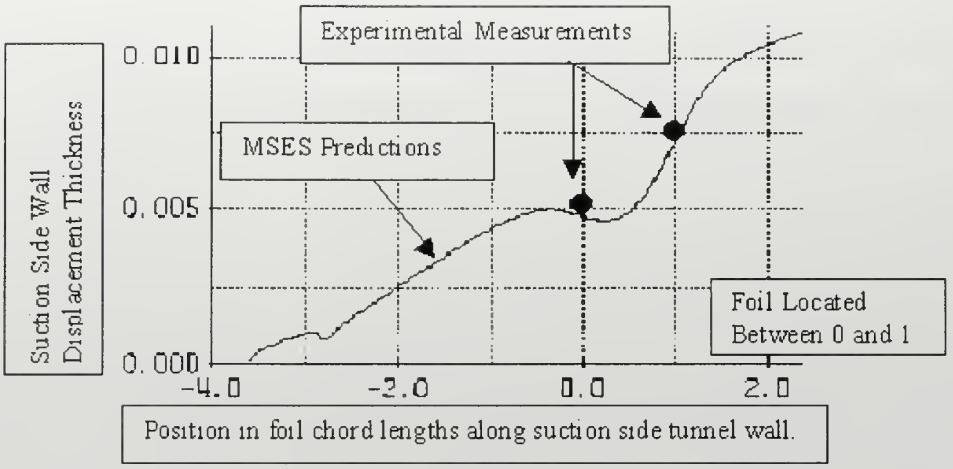

Figure 4-8: Suction Side Tunnel Wall Boundary Layer Measured vs Predicted

parameters and measured lift coefficient were unaffected. The conclusion is that there is no significant interaction between the wall boundary layers and the foil boundary layers.

4.4.3 Tunnel Wall Boundary Layers

It is conceivable that the tunnel wall top and bottom boundary layers would not behave as two dimensional walls due to interactions with the tunnel sidewall boundary layers. In particular, if there were significantly more growth on the suction side wall than predicted, it could result in an effective "decambering" of the foil. This would make the foil seem as if it had less camber than the actual geometry and reduce the experimental lift.

This hypothesis is tested by measuring the tunnel suction side wall boundary layer at the front and back of the foil and comparing these measurements with the predictions of the same parameters in MSES. Figure 4-8 shows that there is good agreement between predicted wall boundary layer behavior and measured wall boundary layer behavior.

4.4.4 Summary

At this point in the analysis of the highly cupped trailing edge geometry the major experimental uncertainties have been addressed, but there is still a very large difference between measured and predicted performance. On the basis of this, it appears the numerical methods are not

satisfactory for this application. If the numerical methods are truly at fault, the errors here are clearly unacceptable. Given the presumption that two dimensional hydrodynamics can be accomplished by computational fluid dynamics regardless of geometry, there is still a hesitancy to trust these results.

Chapter 5

Analysis of Blunt and Streamlined Foil Sections

Based on the previous chapter, computational fluid dynamics and experimental results have important differences that result in drastically different lift predictions for the cupped foil geometry. The question that then arises is whether similar issues exist between CFD and experiments for other types of foil geometries. Experiments are conducted on a variety of foil shapes and computations are performed in MSES.

5.1 Traditional Streamlined Sharp Trailing Edge

The streamlined foil geometry features reduced loading near the leading edge for cavitation performance and a typical unloaded, streamlined and sharp trailing edge. This type of foil would be expected to be relatively easy for CFD codes to predict performance since the angle at which the flow leaves the foil is defined by the streamlined trailing edge. The experiments were conducted by Kimball [4] and the MSES computations were conducted for this thesis. The data taken by Kimball was analyzed using the algorithms applied on the rest of the foils in this experiment and the results were consistent with his conclusions. Figure 5-1 shows that there is almost perfect agreement between measured and predicted lift for this foil. The analysis conducted here validates the accuracy of MSES as well as the experimental setup for traditional foil designs.

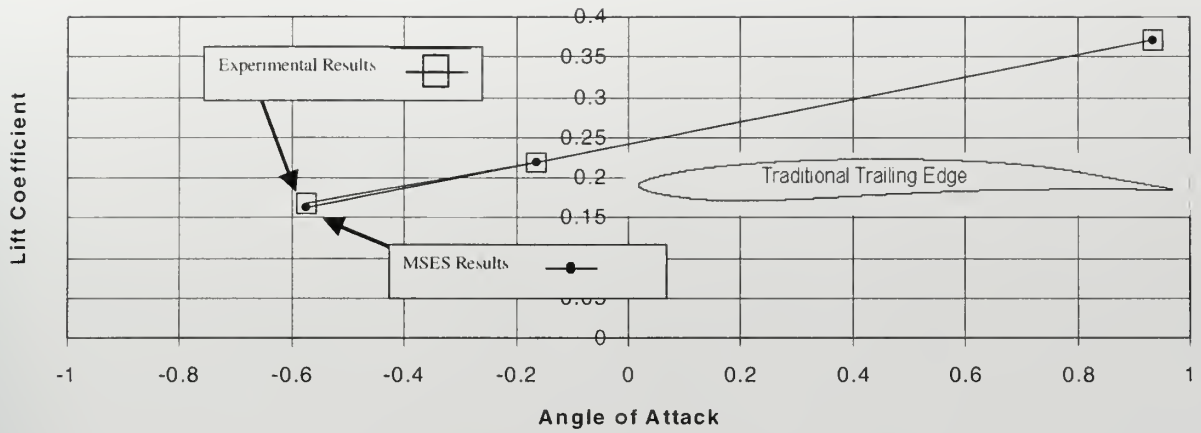

Figure 5-1: Numerical and Experimental Lift for Streamlined Sharp Trailing Edge Foil Geometry

5.2 Blunt Trailing Edge

5.2.1 Numerical and Experimental Results

In the same experiment shown above Kimball conducted an analysis of a foil with a blunt trailing edge as shown in Figure 5-2. This foil was modeled after the parent foil discussed in the previous section, but includes a blunt trailing edge with a height of 2% of the chord length. The results for this foil are not as encouraging. There is significant error introduced due to the blunt trailing edge as shown in Figure 5-2.

Another foil with only a 0.75% of the chord length blunt trailing edge is analyzed in MSES and experimentally. The differences between experimental and CFD predictions for this foil showed even greater error than the foil with more blunting at the trailing edge. The outcome of this analysis is shown in Figure 5-3. It is interesting to note that even though the extent of the blunting is smaller, the disagreement between experiment and CFD is larger. The nature of these results was somewhat surprising and caused the question to arise whether or not the boundary layer method of MSES would give the same results that would be obtained using a Reynolds Averaged Navier Stokes solver.

DTNS2D is a generalized 2-D domain incompressible RANS fluid flow solver developed at the U.S. Naval Surface Warfare Center, Carderock Division. DTNS2D uses a finite volume

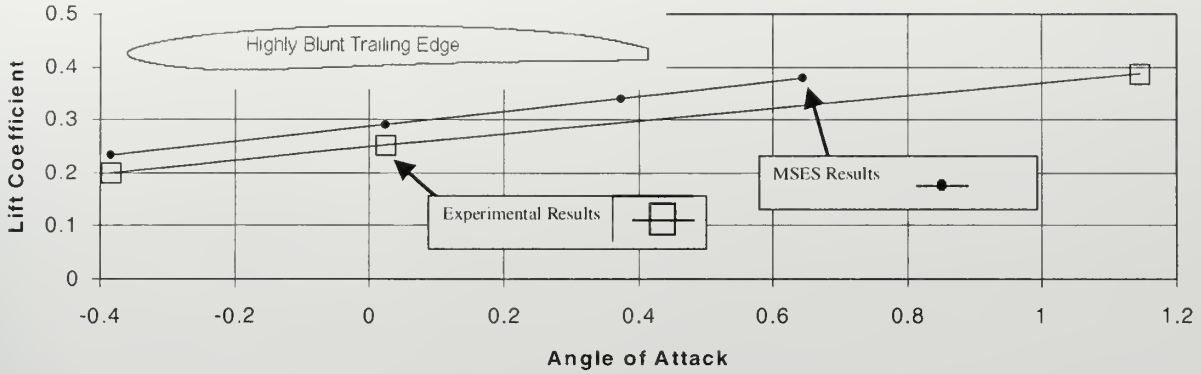

Figure 5-2: Numerical and Experimental Lift for Blunt Trailing Edge Foil Geometry

finite difference formulation. It has been used previously for analyzing traditional surfaces with results that agree with experimental data [11]. The code DTNS2D was developed by Gorski [12]. The code utilizes a third-order upwind difference total-variation-diminishing (TVD) scheme applied to the convection terms and a second-order central difference scheme applied to the diffusion terms. The Baldwin-Lomax turbulence model and K-ε models were both used for the analysis performed here and the results were consistent with 0.004 in lift coefficient.

5.2.2 Analysis

One major difference between the sharp streamlined trailing edge foil and the blunt trailing edge foil geometries is the separated region that occurs just beyond the trailing edge of a blunt foil. The obvious conclusion is that either the accuracy of the experiment, the accuracy of the flow code or the ability to represent the conditions in the flow code with an experiment is effected by this region. Here the latter of these possibilities is explored.

It is possible that due to the change in geometry between the streamlined and blunt trailing edges that the ability to model the conditions used in CFD is lost. In order for this to be true there would need to be a significant global impact on the flow problem due to a very localized feature at the trailing edge. In the case of the cupped foil, this effect was eliminated by installing flow fences to block any communication between the foil boundary layer and the tunnel wall boundary layer.

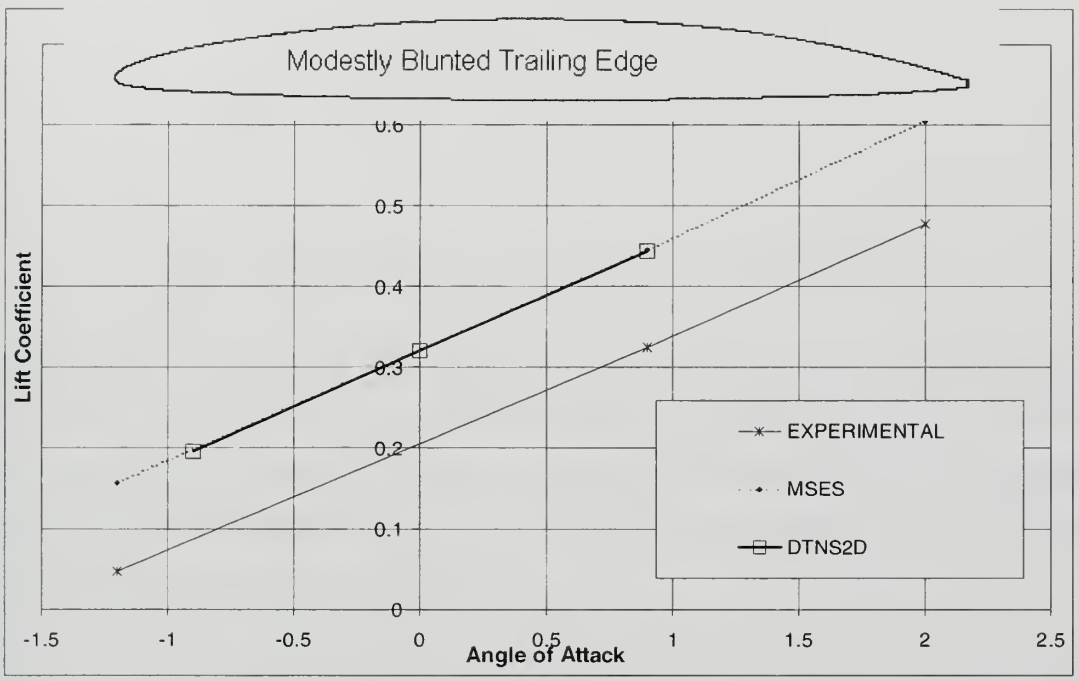

Figure 5-3: Numerical and Experimental Lift for Modestly Blunt Trailing Edge Foil Geometry

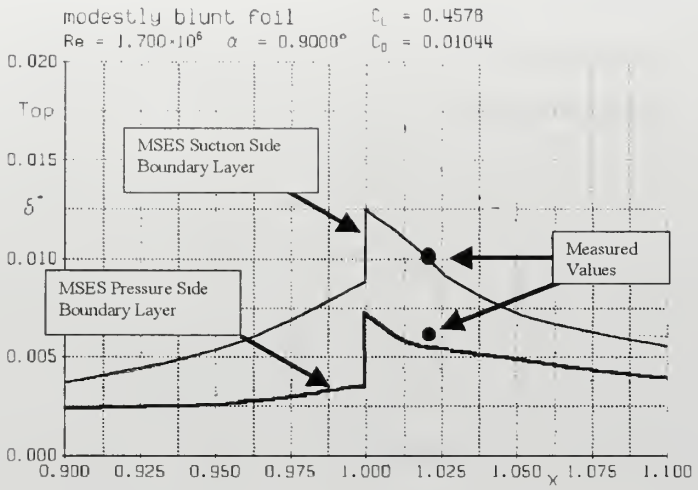

Figure 5-4: Modestly Blunt Foil Boundary Layer Thickness

In the case of the blunt foil, the sensitivity of foil performance to contamination of the boundary layer is studied and the contamination levels are measured. Figure 5-4 shows the predicted boundary layer thickness near the trailing edge from MSES and the experimentally measured boundary layer thicknesses. There seems to be good agreement between the experiment and predicted boundary layer thicknesses.

In order to measure the sensitivity of foil performance to contamination of the boundary layer, false sources are placed in the separated region behind the foil. These sources are adjusted in magnitude until the lift coefficient realized in the experiment is matched. Another method of increasing the boundary layer thickness is reducing the Reynolds Number. When the Reynolds Number is reduced to $2*10^4$ the lift coefficient predicted agrees with the experimental lift coefficient. Figure 5-5 shows the boundary layer displacement thickness predicted each way as well as the physically measured boundary layer thickness. It is clear that the measured value is closest to the MSES predicted boundary layer with no contamination at the appropriate Reynolds Number. This seems to indicate that although the predicted lift is wrong, the boundary layer calculations in MSES are functioning well. Based on this it would seem that

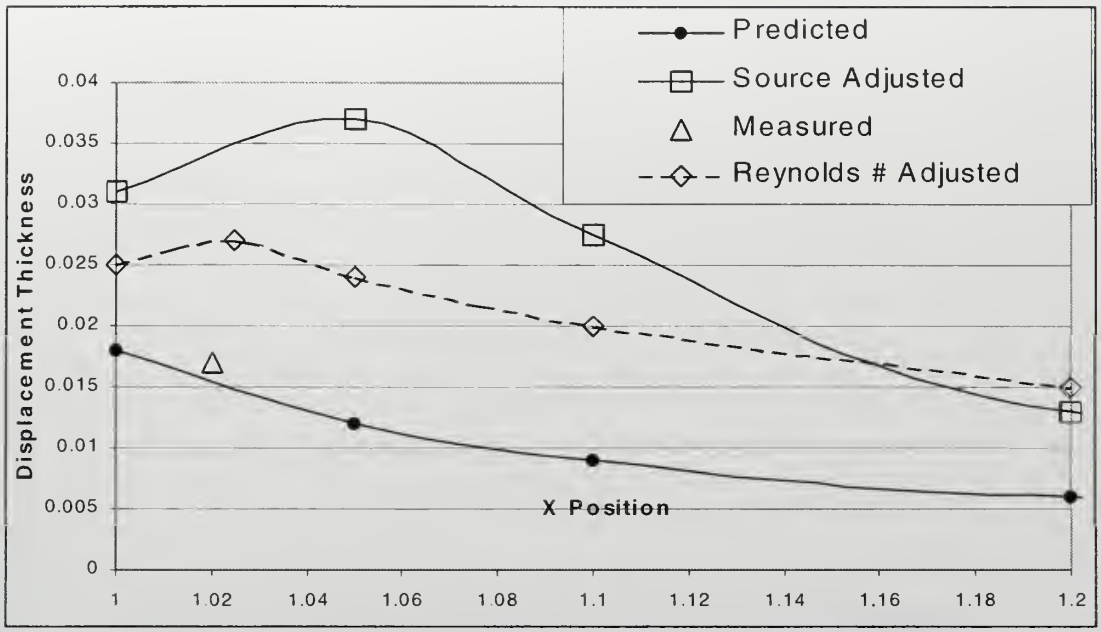

Figure 5-5: Wake Displacement Thicknesses Assuming Various Experimental Errors

the tunnel is still providing a two dimensional environment for the foil to operate in.

5.2.3 Effectiveness of Boundary Layer Trips

Boundary layer trips are placed on the foil at 10% of the chord length to cause transition to a turbulent boundary layer. These trips are simulated in MSES by tripping the boundary layer at 10% of the chord length. If these trips were ineffective it could conceivably effect the boundary layer size and therefore lift. This concept is explored on the modestly blunt trailing edge foil. Table 5.1 shows the variation in predicted lift coefficient for the conditions stated. It is also possible that the tunnel turbulence would force an almost immediate turbulent boundary layer which is modeled by putting the forced trip at the 1% position. These variations are small compared and generally in the wrong direction when compared to the experimental results.

Suction Side Trip	Pressure Side Trip	Lift Coefficient
forced (0.1)	forced (0.1)	0.326
natural (0.86)	forced (0.1)	0.409
natural (0.86)	natural (0.95)	0.389
forced (0.1)	natural (0.95)	0.301
forced (0.01)	forced (0.01)	0.3244
EXPERIMENT	both forced (0.1)	0.205

Table 5.1: Lift Coefficient verses Turbulence Stimulator Effectiveness

Chapter 6

Conclusions

It has been shown in this thesis that experimental results for a two dimensional foil are accurate and repeatable. Many areas of uncertainty have been analyzed and none of the uncertainties can explain the inconsistencies between numerical and experimental foil performance. Based on these results, the following is a summary of the capabilities and limitations of CFD in predicting two dimensional foil performance:

1. CFD is fully capabile of predicting performance of traditional foils with sharp unloaded trailing edges including cambered and symmetric designs.

2. CFD is fully capabile of predicting performance of blunt trailing edge foils with no camber loading.

3. CFD effectively predicts lift slope for asymmetric blunt trailing edge foils.

4. [1]CFD over predicts the contribution of camber on asymmetric blunt trailing edge foils.

5. [1] CFD over predicts the contribution of camber on foils with premature separation due to excessive trailing edge curvature.

[1]The offset in angle of attack is somewhat of a mystery, but a very significant effect. Continuing research will go into this area. The outstanding agreement between RANS codes and boundary layer codes seem to indicate that there is a common assumption between these programs that is in error. One current notion is that the organized asymmetric vortex shedding that goes along with a cambered separated trailing edge has a mean effect on the lift. If this were true, it may not be captured in a time average code.

6. [2]CFD over predicts the lift slope on foils with premature separation due to excessive trailing edge curvature.

[2]The inaccuracy in lift slope is most likely caused by incorrect prediction of the movement of the separation point as the angle of attack changes.

Bibliography

[1] J. Jorde, A Study of Two Cambered Trailing Edge Geometries, Master's thesis, Massachusetts Institute of Technology, Cambridge, MA, 1995.

[2] H. Schlichting, *Boundary Layer Theory*, McGraw-Hill, New York, 1955.

[3] S. A. Kinnas, Hydrofoil Lift and Drag from Momentum Integrations, Engineering Report 91-4, Technical report, MIT Ocean Engineering, Cambridge, MA, 1991.

[4] R. Kimball and D. Egnor, HRA 2D Foil Experiment, Technical report, MIT Ocean Engineering, Cambridge, MA, 1997.

[5] G. VanWylen and R. Sonntag, *Fundamentals of Classical Thermodynamics*, John Wiley and Sons, New York, 1965.

[6] C. M. Prieto, Drag Force Measurement Using Momentum Integration: Experimental and Analytical Results, 1998.

[7] J. N. Newman, *Marine Hydrodynamics*, MIT Press, 1977.

[8] C. H. Sung and M. J. Griffin, Improvements in Incompressible Turbulent Horseshoe Vortex Juncture Flow Calculations, Technical report, 29th Aerospace Sciences Meeting, Reno, Nevada, 1996.

[9] M. Drela, Integral Boundary Layer Formulation for Blunt Trailing Edges, AIAA paper **89-2200** (1989).

[10] D. C. Wilcox, Turbulence Modeling for CFD, Technical report, DCW Industries, Inc., CA, 1993.

[11] P. Nguyen and J. Gorski, Navier-Stokes Analysis of Turbulent Boundary Layer and Wake for Two-Dimensional Lifting Bodies, in *Proceedings of the Eighteenth Symposium on Naval Hydrodynamics*, pages 633–644, Office of Naval Research, January 1991.

[12] J. J. Gorski. Multiple Block Calculations of the Navier-Stokes Equations for Incompressible Flows, in *Proceedings of the* 12^{th} *U.S.-Federal Republic of Germany Data Exchange Meeting*, Bethesda, MD USA, 1988.

Appendix A

Water Tunnel Three Dimensional Effects

Figure (A-1) shows the effect of side wall boundary layer growth on control volume measurements. In a two dimensional control volume (shown in Figure (A-2)) the change in momentum between the fluid entering and leaving the control volume is measured at the boundaries to determine the net force on the control volume. These calculations utilize a unit thickness dz for determining the mass flow into and out of the control volume. If there is any net flow into or out of the control volume from the sides, this is not taken into account by this boundary calculation.

A "typical" boundary layer growth of $5mm$ over the length of the control volume is considered. The tunnel width is $500mm$, so the boundary layer growth represents 2% of the total tunnel width. Based on the side wall boundary layer growth alone an increase in momentum of 2% is expected. The view of the control volume in Figure (A-2) is considered. This side of the control volume has a top and a bottom that follow a streamline in this plane. There is a net reduction in momentum of fluid in this plane based on the viscous friction with the surfaces of the foil. For a typical drag coefficient of $C_D = 0.01$ and a typical control volume height of $\frac{1}{3}$ of the height of the tunnel there is a momentum deficit caused by the foil of 1.5%.

The velocity and quantity of flow into the sides of a control volume are difficult to predict and cause significant sources of errors. It has been shown here that these sources of errors are

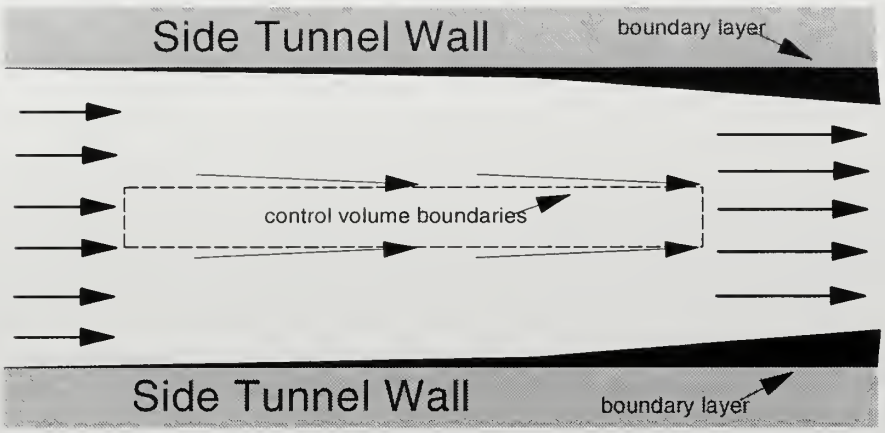

Figure A-1: Depiction of Two Dimensional Control Volume on Edge

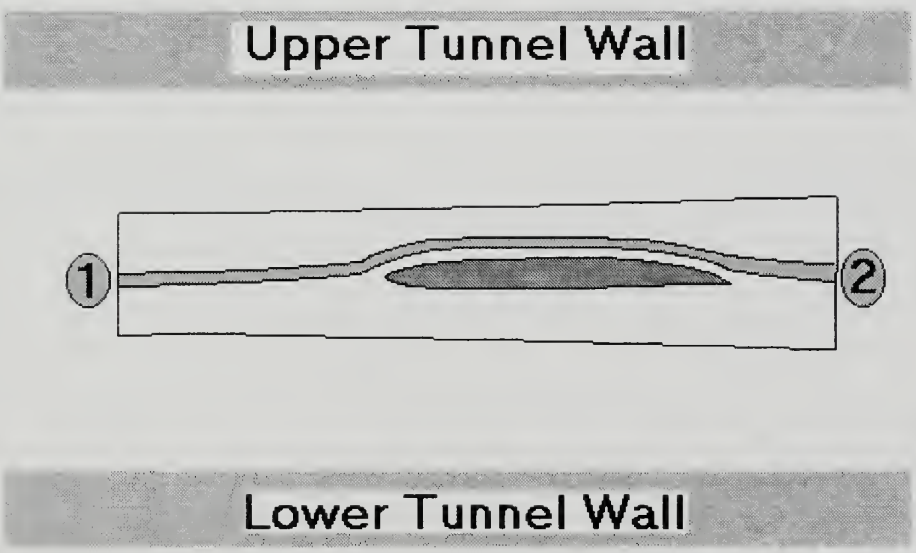

Figure A-2: Control Volume Considered for Analysis

on the same order of magnitude as the parameters being measured. This explains why it has been the consistent experience at MIT that the control volume measurement of drag forces is unreliable and sometimes even shows a net thrust!

Appendix B

Laser Doppler Velocimetry Data

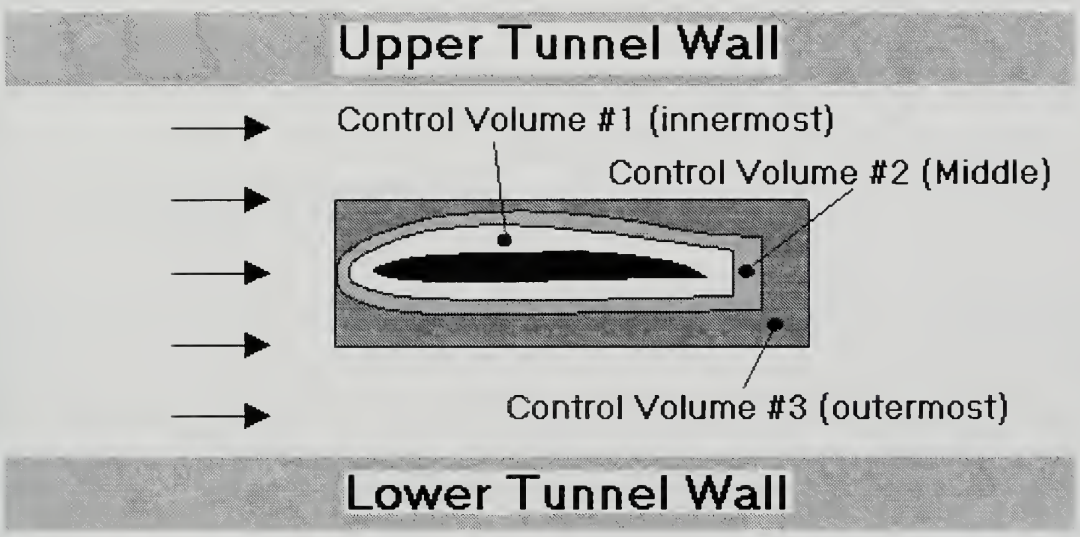

Figure B-1: Data Summary Key

Figure B-1 shows the geometry of the control volume data plotted. Each of the plots (Figures (B-2), (B-3) and (B-4)) shows the properties indicated verses path length along the control volume. The data is plotted counter clockwise starting at the lower right hand corner of each control volume.

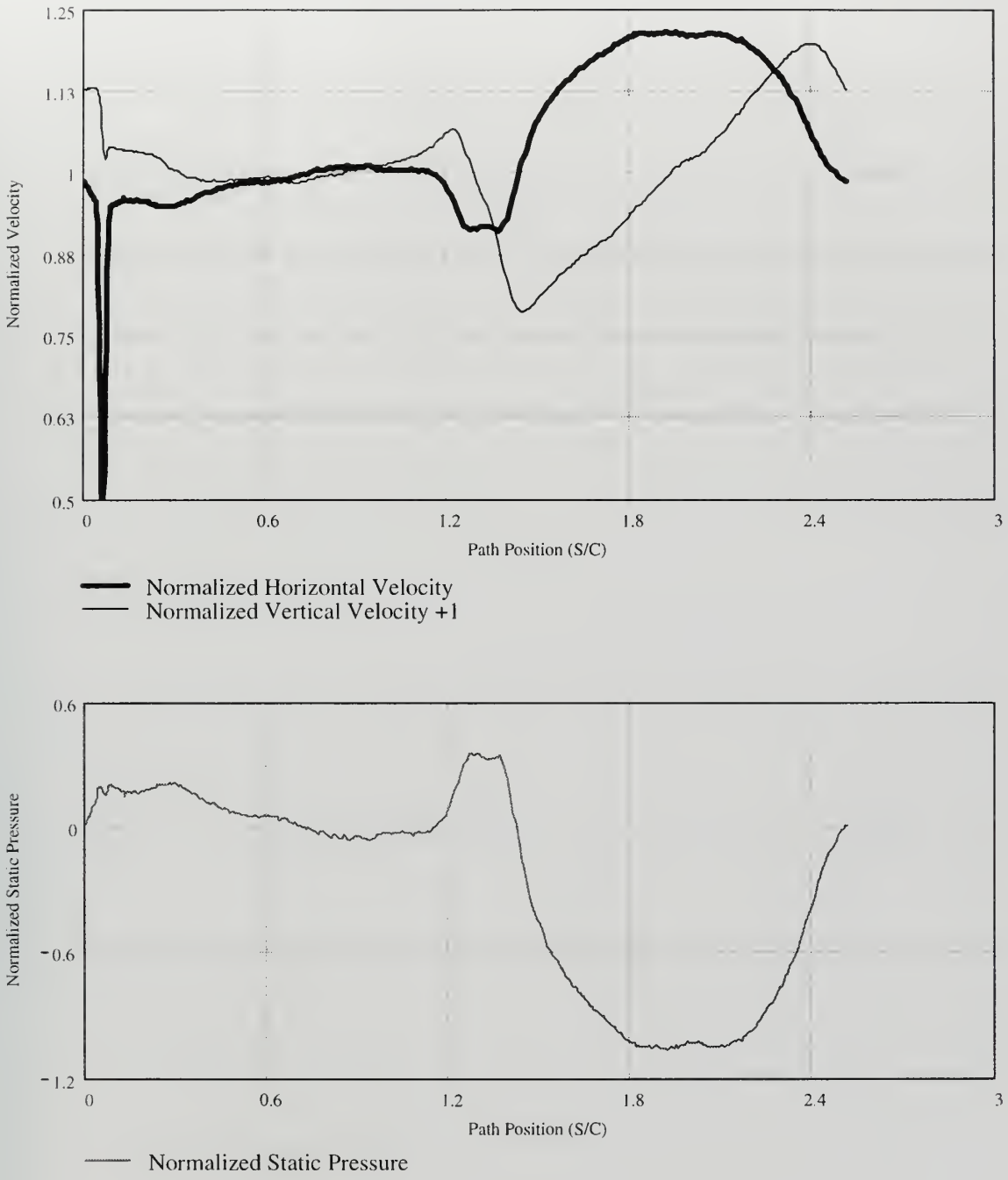

Figure B-2: Control Volume #1 Raw Data

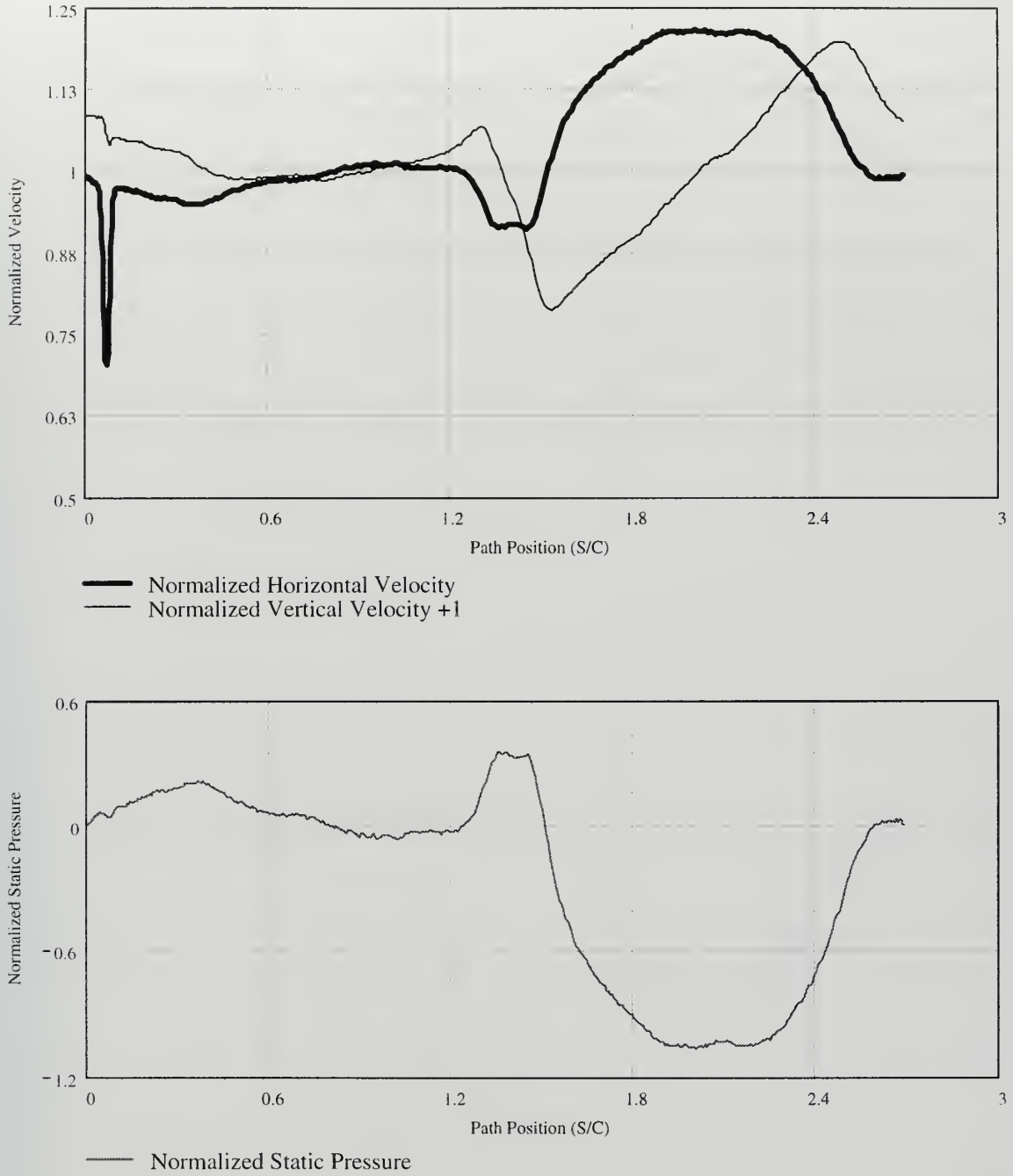

Figure B-3: Control Volume #2 Raw Data

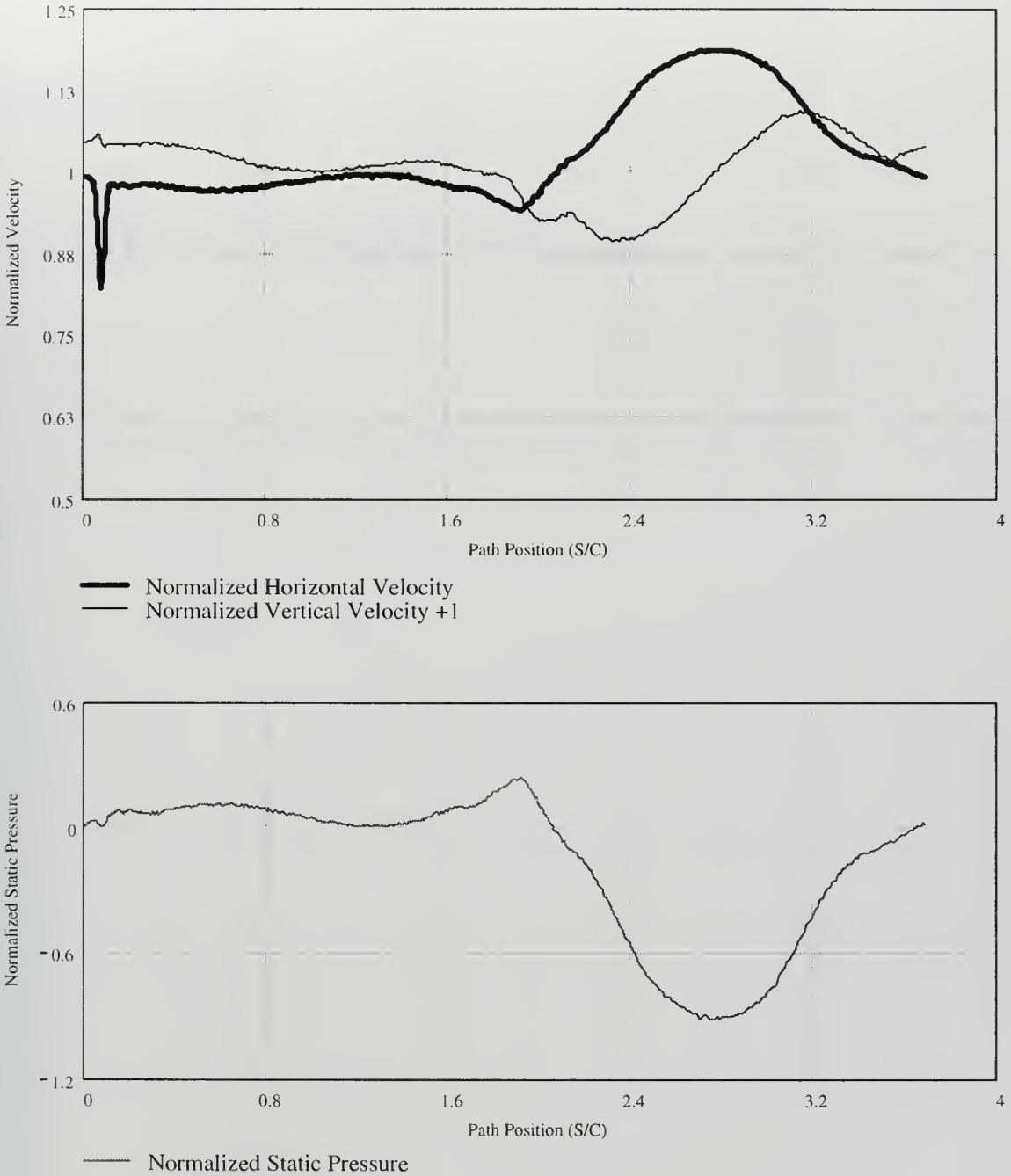

Figure B-4: Control Volume #3 Raw Data

Appendix C

PIV Experimental Data

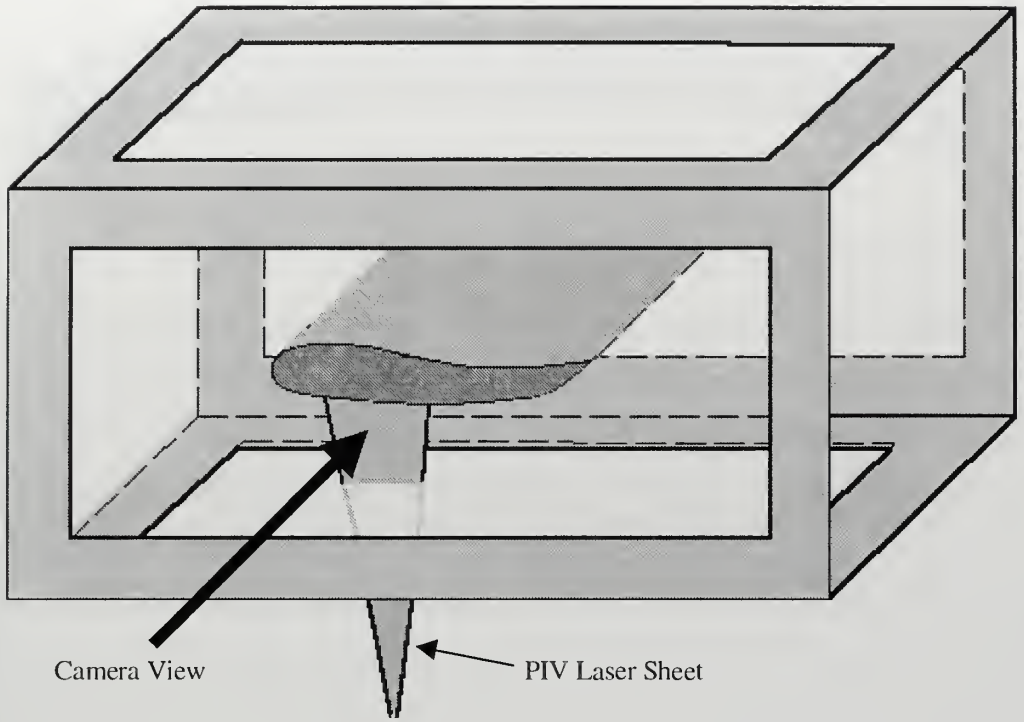

Figure C-1: Particle Image Velocimetry Experimental Setup

Particle image velocimetry is an experimental method which consists of lighting a plane of fluid containing flourescent particles with a laser sheet and taking pictures of their position with a camera. Two pictures are taken close in time with one another and the distance of the movement of the particles between laser pulses combined with a known time between laser pulses gives a snapshot of the velocity at an instant in time. For this experiment the time between laser pulses was 0.037 milliseconds and the camera area covered was about 5 centimeters. Figure C-1 shows the experimental setup used for these PIV measurements. Measurements are only taken on the suction side of the foil in this portion of the experiment.

The particle image velocimetry measurements at each instant in time are averaged to provide a mean velocity. In this experiment only 126 individual velocity values were used to determine the average. It is clear from laser doppler velocimetry experience that 126 samples in an average is not sufficient to provide a reliable mean value in turbulent areas. Another weakness of the particle image velocimetry measurements in this experiment is that each sample was taken in a

Figure C-2: Summary of PIV Data Including Pressure Contours

single burst of laser pulses and pictures. This means that any tunnel speed fluctuations at low frequency (on the order of seconds) will show up in the particle image velocimetry measurements as a shift in the mean values for the particular sample. In short, the mean values of the particle image velocimetry measurements in this experiment are suspect, but the trends shown in each sample are likely to be reliable.

Figure C-2 shows the datafield considered in the particle image velocimetry portion of the experiment. The contours shown are pressure contours. The boundaries shown are the individual pictures that were taken of the different foil sections. Discontinuities from one picture to the next are caused by the variations mentioned above. Each of these pictures contains a 128 by 128 grid of horizontal and vertical velocity at each particular location considered.

The following diagrams are plots of the boundary layer parameters from the various sources that are available. The PIV boundary layers have been scaled to match the projected LDV measurements since the mean value of the LDV measurements are highly reliable. These diagrams are discussed further in the body of this thesis.

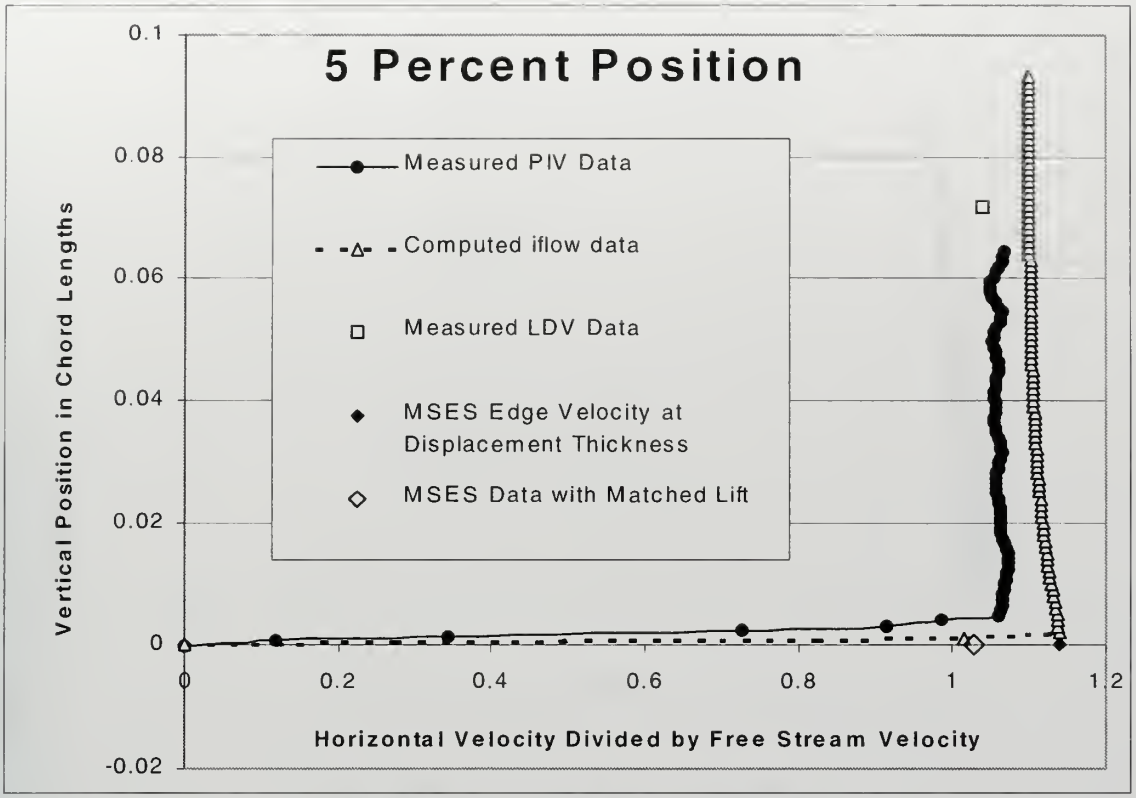
5 Percent Position
Measured PIV Data
Computed iflow data
Measured LDV Data
MSES Edge Velocity at Displacement Thickness
MSES Data with Matched Lift
Vertical Position in Chord Lengths
Horizontal Velocity Divided by Free Stream Velocity
0.1
0.08
0.06
0.04
0.02
0
-0.02
0
0.2
0.4
0.6
0.8
1
1.2

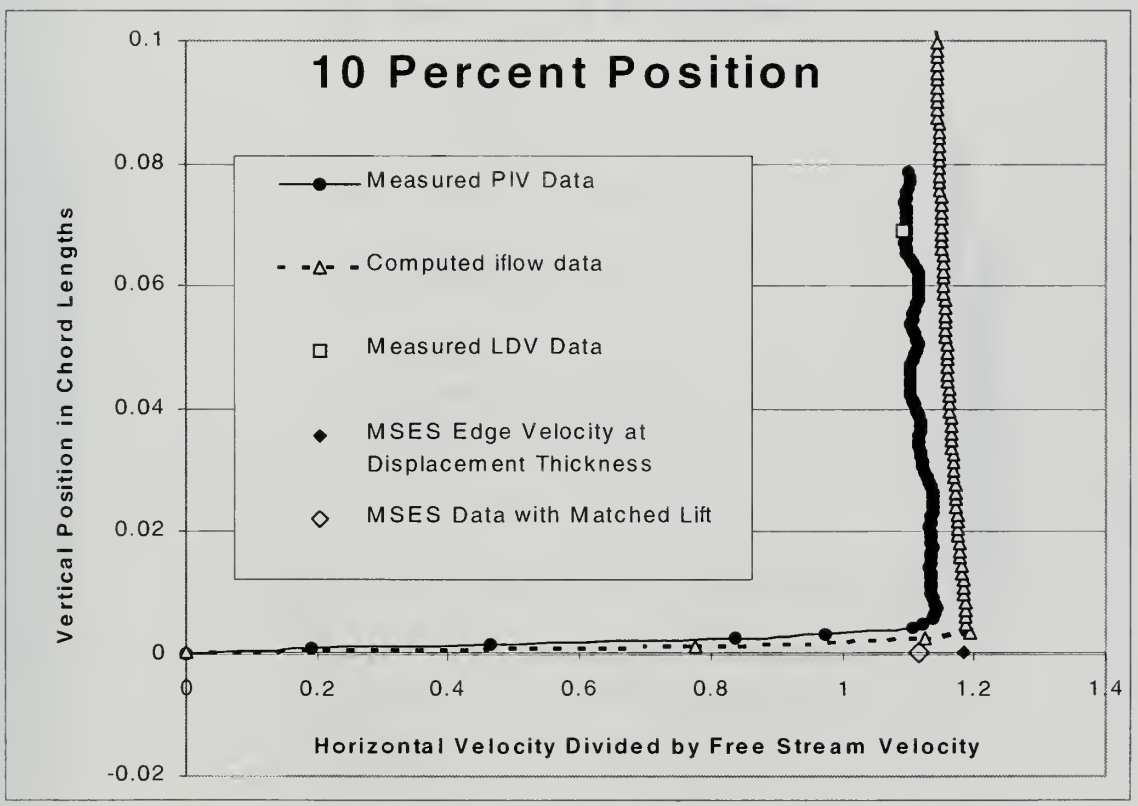
10 Percent Position
Measured PIV Data
Computed iflow data
Measured LDV Data
MSES Edge Velocity at Displacement Thickness
MSES Data with Matched Lift
Vertical Position in Chord Lengths
Horizontal Velocity Divided by Free Stream Velocity
0.1
0.08
0.06
0.04
0.02
0
-0.02
0
0.2
0.4
0.6
0.8
1
1.2
1.4

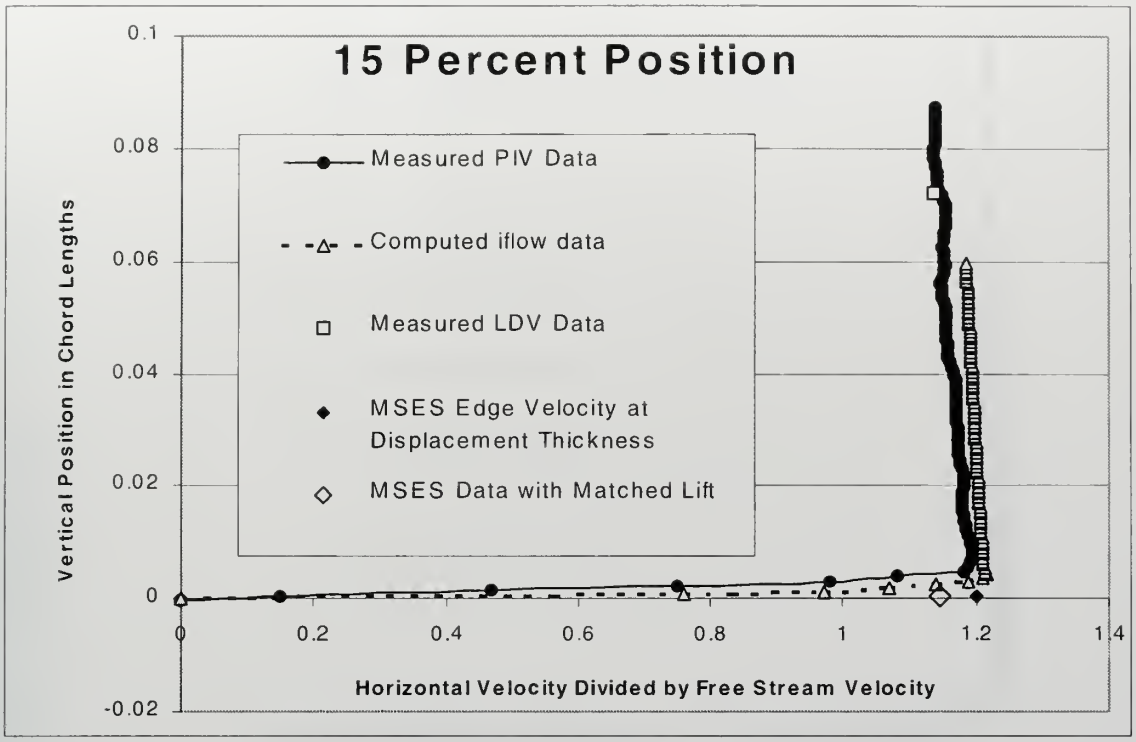
15 Percent Position
Measured PIV Data
Computed iflow data
Measured LDV Data
MSES Edge Velocity at Displacement Thickness
MSES Data with Matched Lift
Vertical Position in Chord Lengths
Horizontal Velocity Divided by Free Stream Velocity
0.1
0.08
0.06
0.04
0.02
0
-0.02
0
0.2
0.4
0.6
0.8
1
1.2
1.4

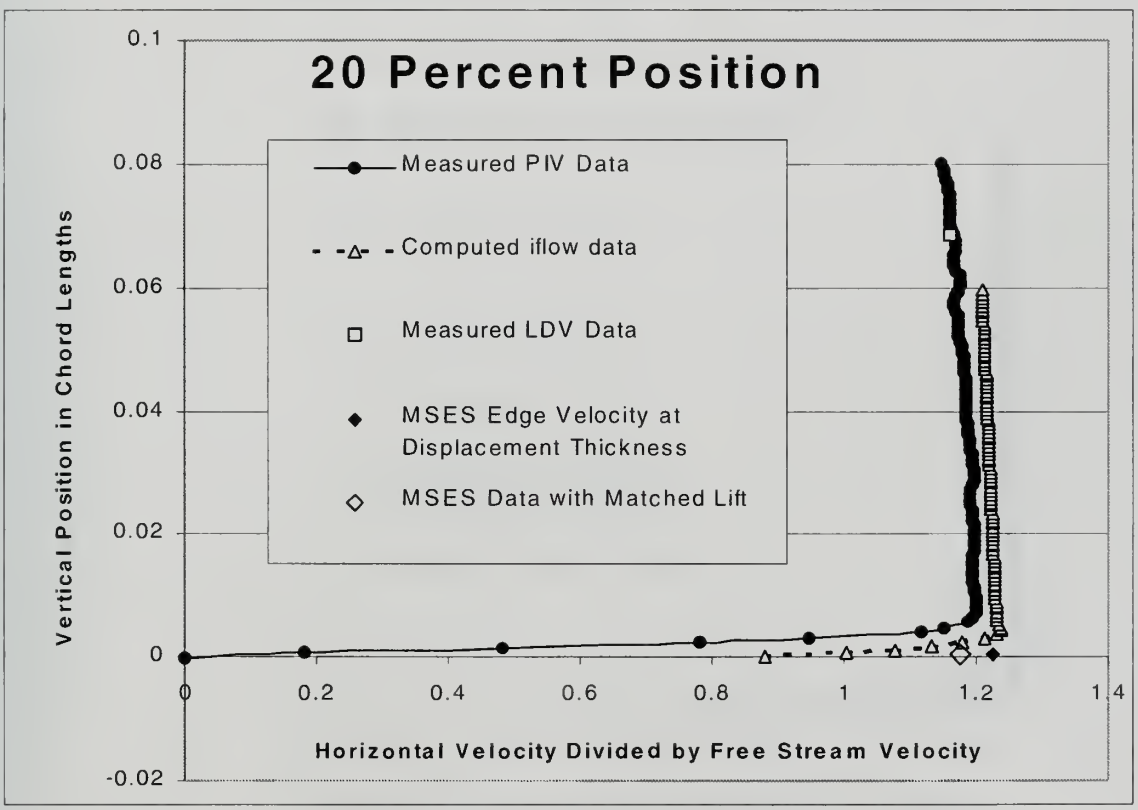
20 Percent Position
Measured PIV Data
Computed iflow data
Measured LDV Data
MSES Edge Velocity at Displacement Thickness
MSES Data with Matched Lift
Vertical Position in Chord Lengths
Horizontal Velocity Divided by Free Stream Velocity
0.1
0.08
0.06
0.04
0.02
0
-0.02
0
0.2
0.4
0.6
0.8
1
1.2
1.4

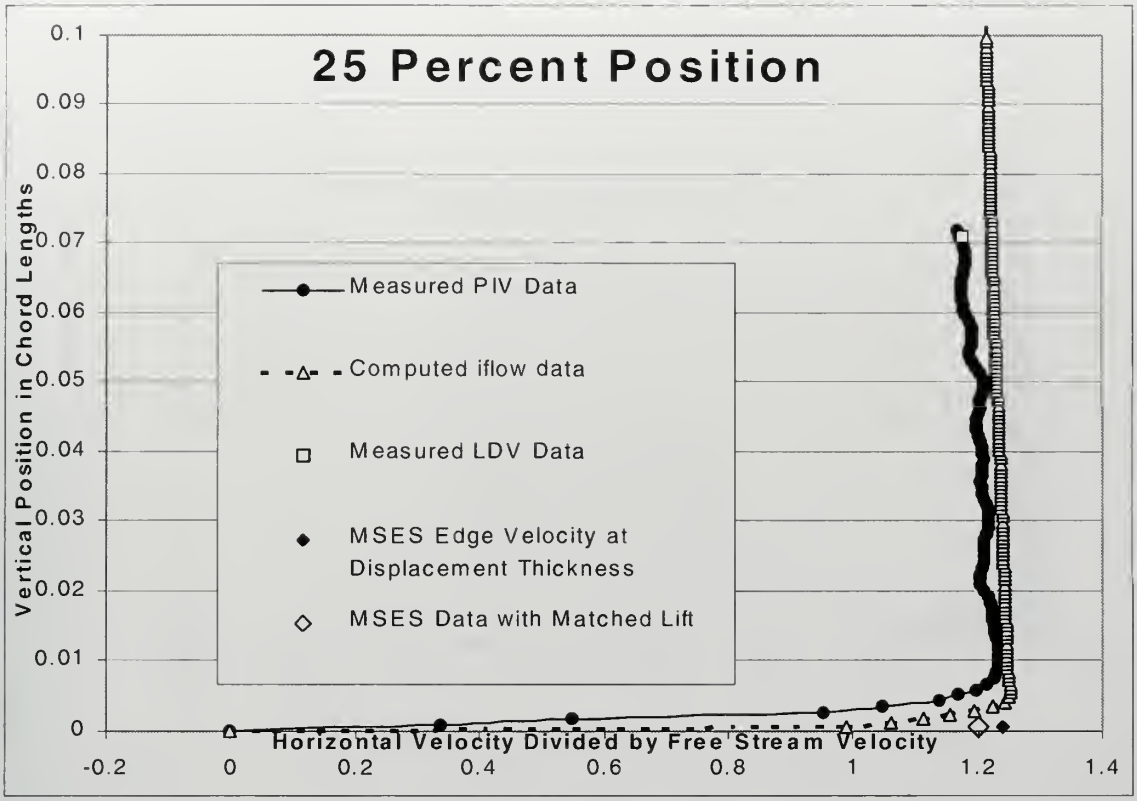
25 Percent Position
Measured PIV Data
Computed iflow data
Measured LDV Data
MSES Edge Velocity at Displacement Thickness
MSES Data with Matched Lift
Vertical Position in Chord Lengths
Horizontal Velocity Divided by Free Stream Velocity
0.1
0.09
0.08
0.07
0.06
0.05
0.04
0.03
0.02
0.01
0
-0.2
0
0.2
0.4
0.6
0.8
1
1.2
1.4

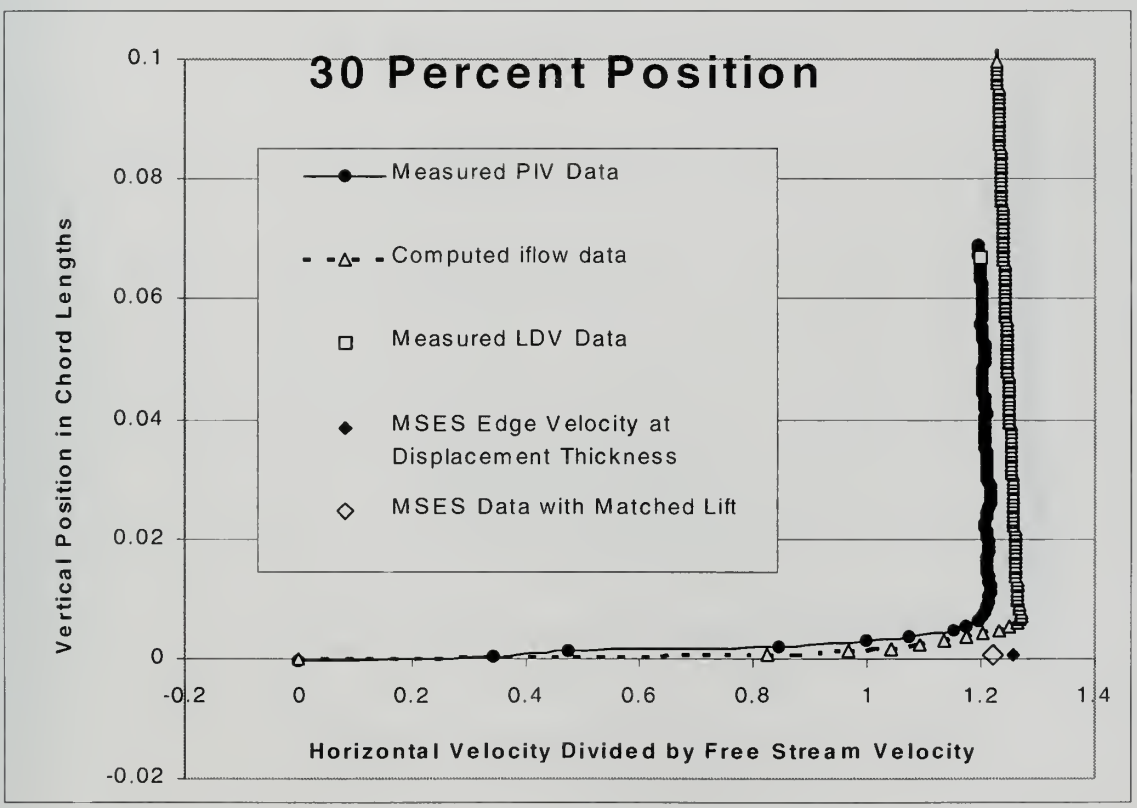
30 Percent Position
Measured PIV Data
Computed iflow data
Measured LDV Data
MSES Edge Velocity at Displacement Thickness
MSES Data with Matched Lift
Vertical Position in Chord Lengths
Horizontal Velocity Divided by Free Stream Velocity
0.1
0.08
0.06
0.04
0.02
0
-0.02
-0.2
0
0.2
0.4
0.6
0.8
1
1.2
1.4

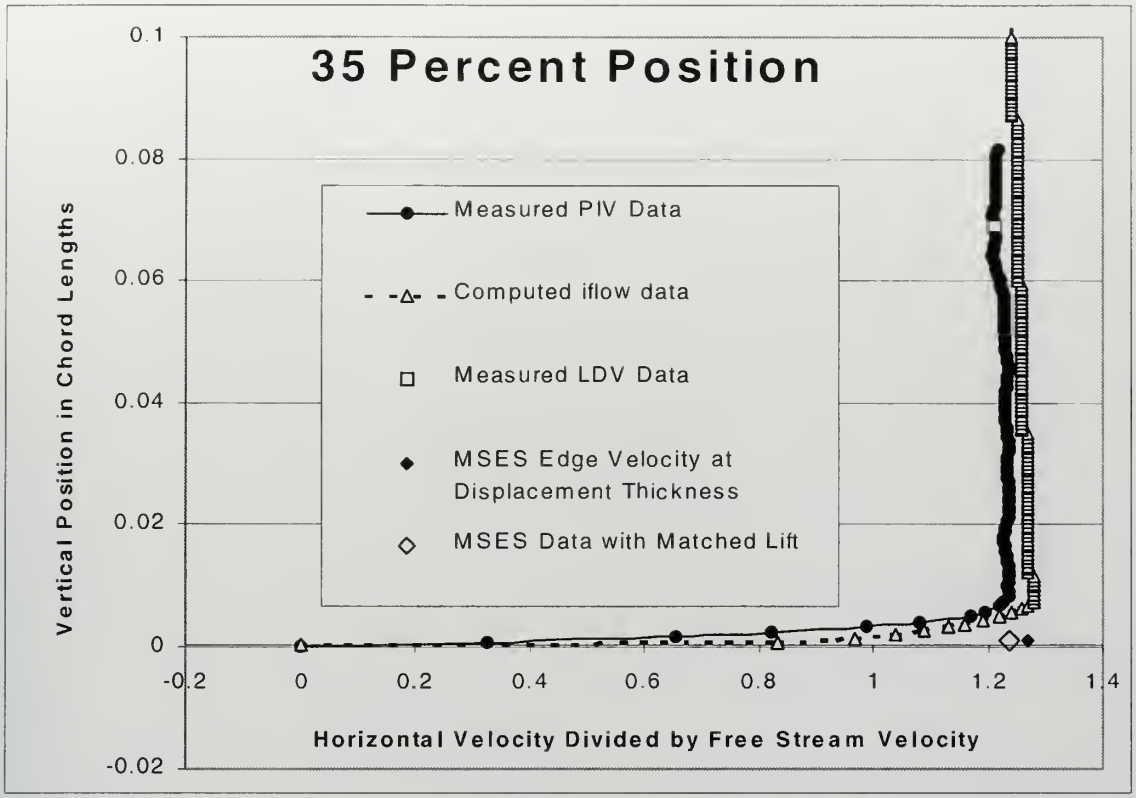
35 Percent Position
Measured PIV Data
Computed iflow data
Measured LDV Data
MSES Edge Velocity at Displacement Thickness
MSES Data with Matched Lift
Vertical Position in Chord Lengths
Horizontal Velocity Divided by Free Stream Velocity
0.1
0.08
0.06
0.04
0.02
0
-0.02
-0.2
0
0.2
0.4
0.6
0.8
1
1.2
1.4

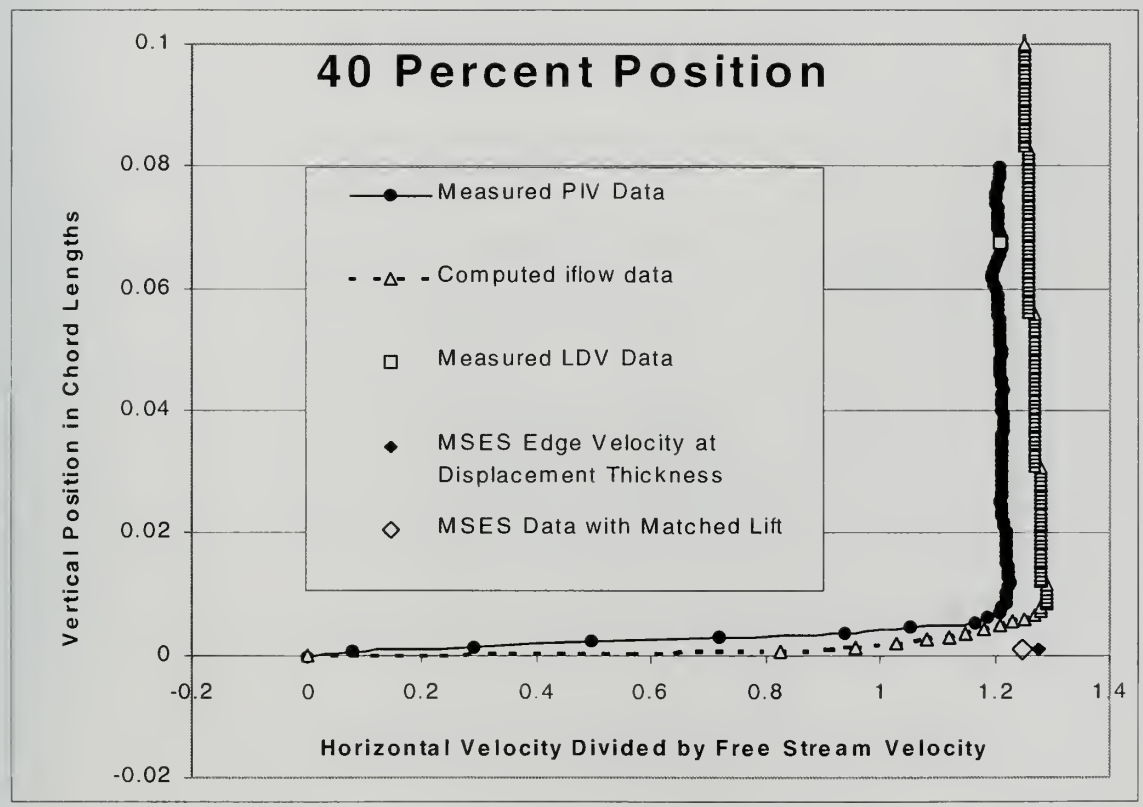
40 Percent Position
Measured PIV Data
Computed iflow data
Measured LDV Data
MSES Edge Velocity at Displacement Thickness
MSES Data with Matched Lift
Vertical Position in Chord Lengths
Horizontal Velocity Divided by Free Stream Velocity
0.1
0.08
0.06
0.04
0.02
0
-0.02
-0.2
0
0.2
0.4
0.6
0.8
1
1.2
1.4

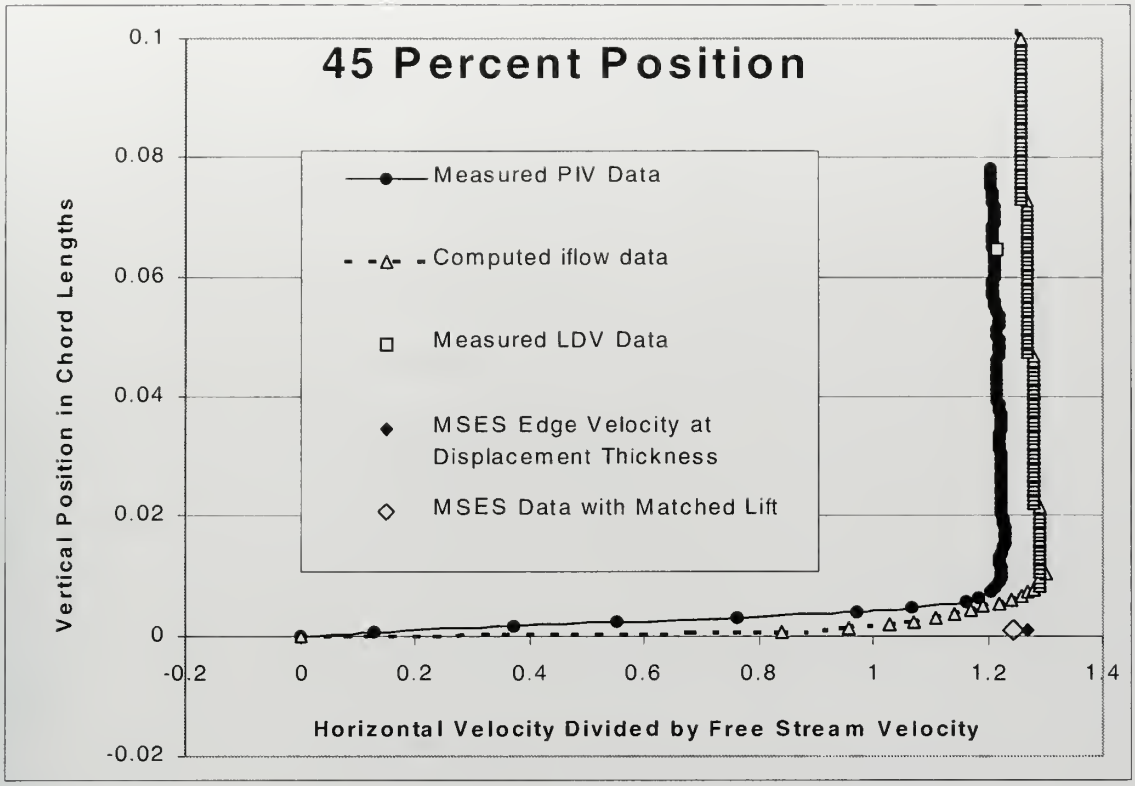
45 Percent Position
Measured PIV Data
Computed iflow data
Measured LDV Data
MSES Edge Velocity at Displacement Thickness
MSES Data with Matched Lift
Vertical Position in Chord Lengths
Horizontal Velocity Divided by Free Stream Velocity
0.1
0.08
0.06
0.04
0.02
0
-0.02
-0.2
0
0.2
0.4
0.6
0.8
1
1.2
1.4

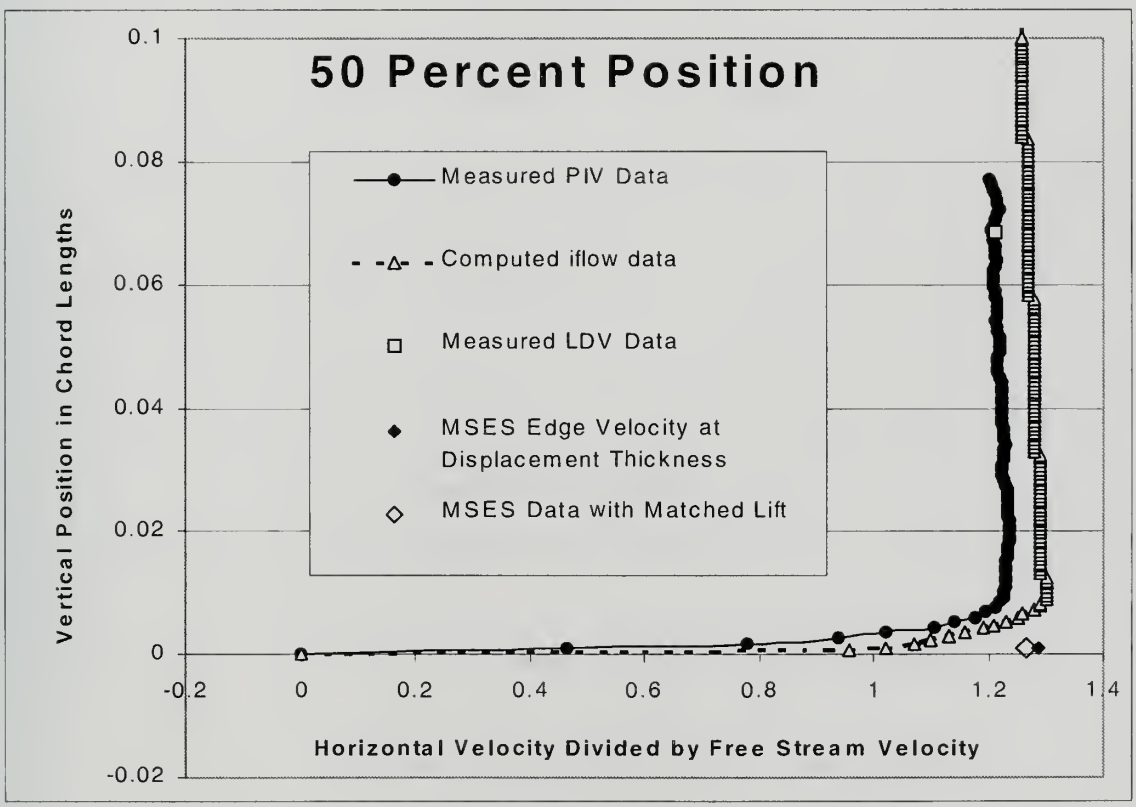
50 Percent Position
Measured PIV Data
Computed iflow data
Measured LDV Data
MSES Edge Velocity at Displacement Thickness
MSES Data with Matched Lift
Vertical Position in Chord Lengths
Horizontal Velocity Divided by Free Stream Velocity
0.1
0.08
0.06
0.04
0.02
0
-0.02
-0.2
0
0.2
0.4
0.6
0.8
1
1.2
1.4

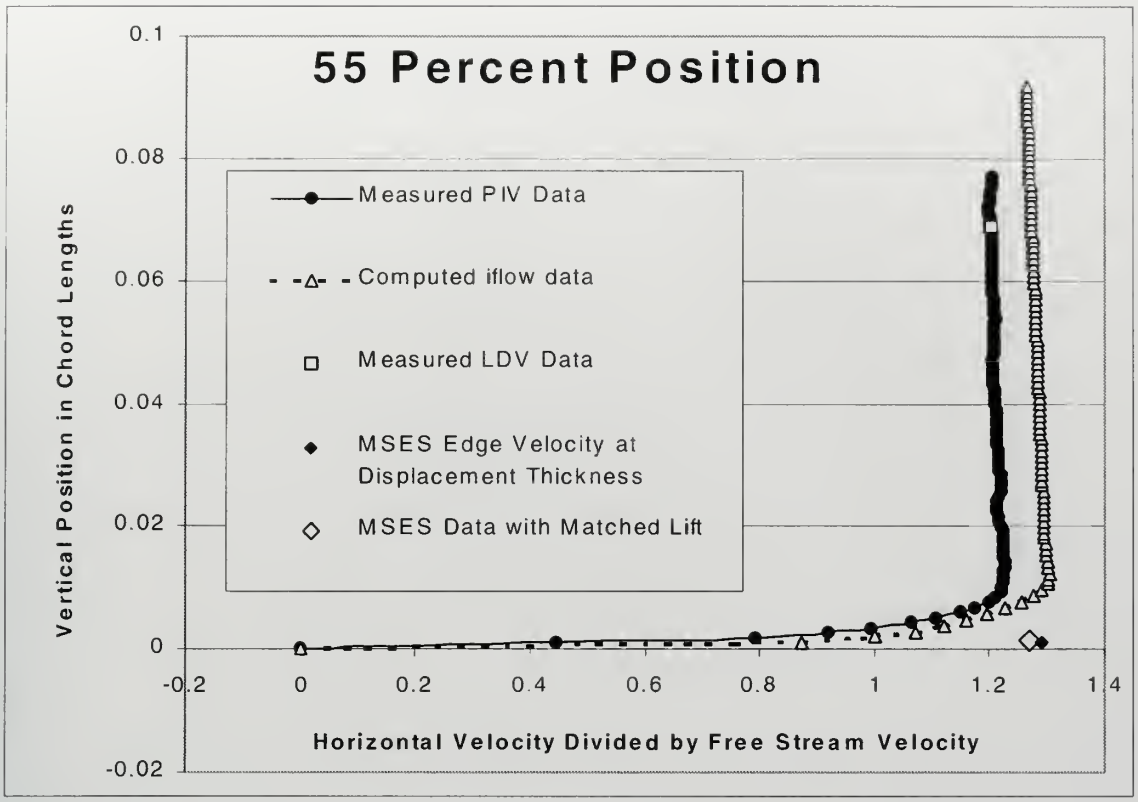
55 Percent Position
Measured PIV Data
Computed iflow data
Measured LDV Data
MSES Edge Velocity at Displacement Thickness
MSES Data with Matched Lift
Vertical Position in Chord Lengths
Horizontal Velocity Divided by Free Stream Velocity
0.1
0.08
0.06
0.04
0.02
0
-0.02
-0.2
0
0.2
0.4
0.6
0.8
1
1.2
1.4

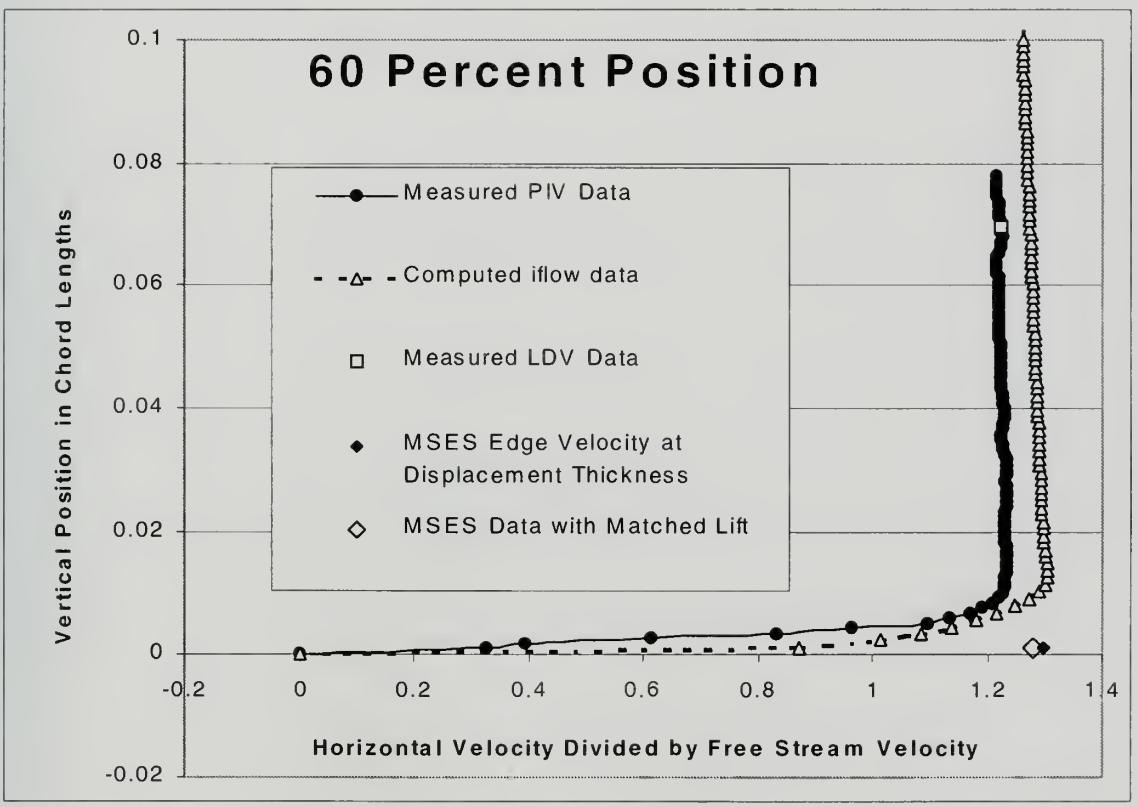
60 Percent Position
Measured PIV Data
Computed iflow data
Measured LDV Data
MSES Edge Velocity at Displacement Thickness
MSES Data with Matched Lift
Vertical Position in Chord Lengths
Horizontal Velocity Divided by Free Stream Velocity
0.1
0.08
0.06
0.04
0.02
0
-0.02
-0.2
0
0.2
0.4
0.6
0.8
1
1.2
1.4

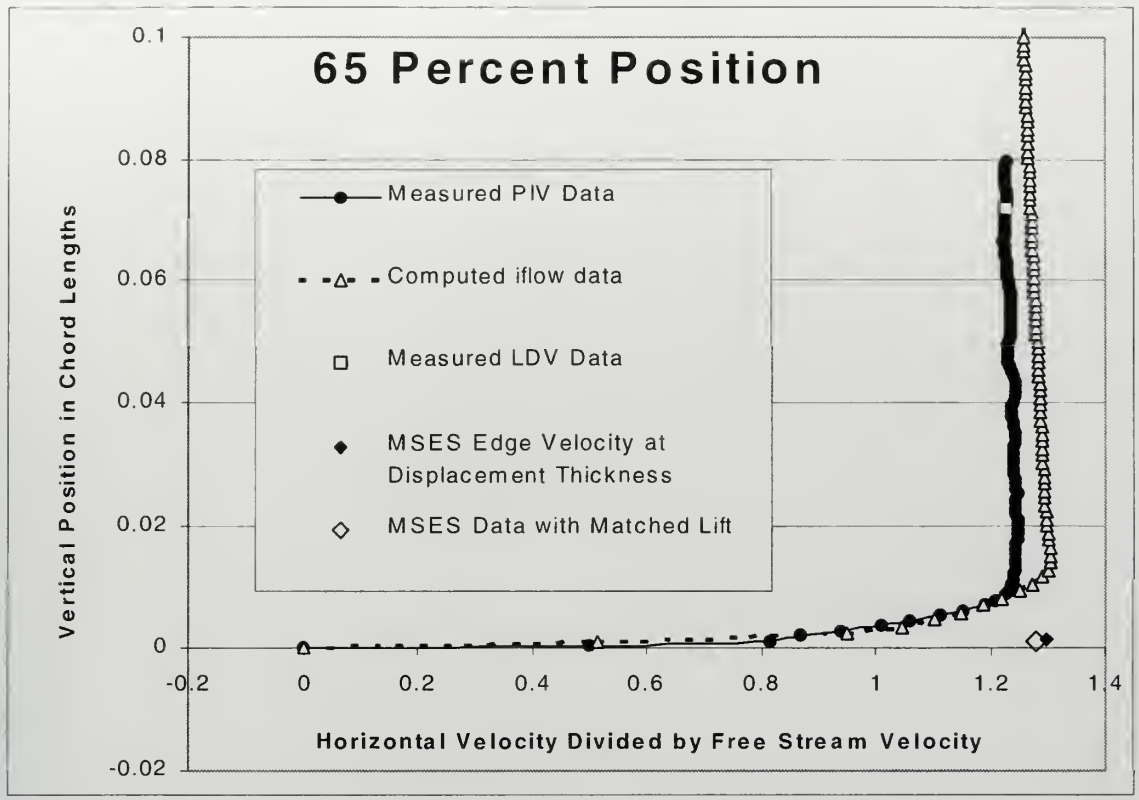
65 Percent Position
Measured PIV Data
Computed iflow data
Measured LDV Data
MSES Edge Velocity at Displacement Thickness
MSES Data with Matched Lift
Vertical Position in Chord Lengths
Horizontal Velocity Divided by Free Stream Velocity
0.1
0.08
0.06
0.04
0.02
0
-0.02
-0.2
0
0.2
0.4
0.6
0.8
1
1.2
1.4

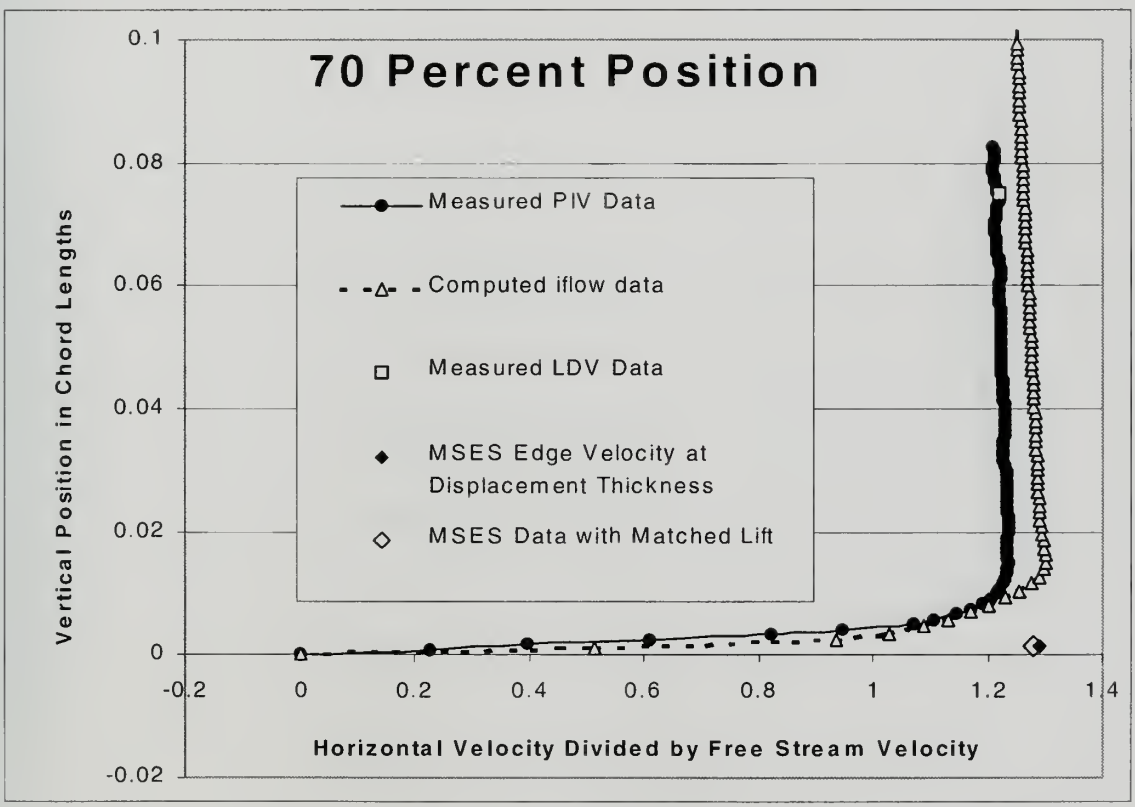
70 Percent Position
Measured PIV Data
Computed iflow data
Measured LDV Data
MSES Edge Velocity at Displacement Thickness
MSES Data with Matched Lift
Vertical Position in Chord Lengths
Horizontal Velocity Divided by Free Stream Velocity
0.1
0.08
0.06
0.04
0.02
0
-0.02
-0.2
0
0.2
0.4
0.6
0.8
1
1.2
1.4

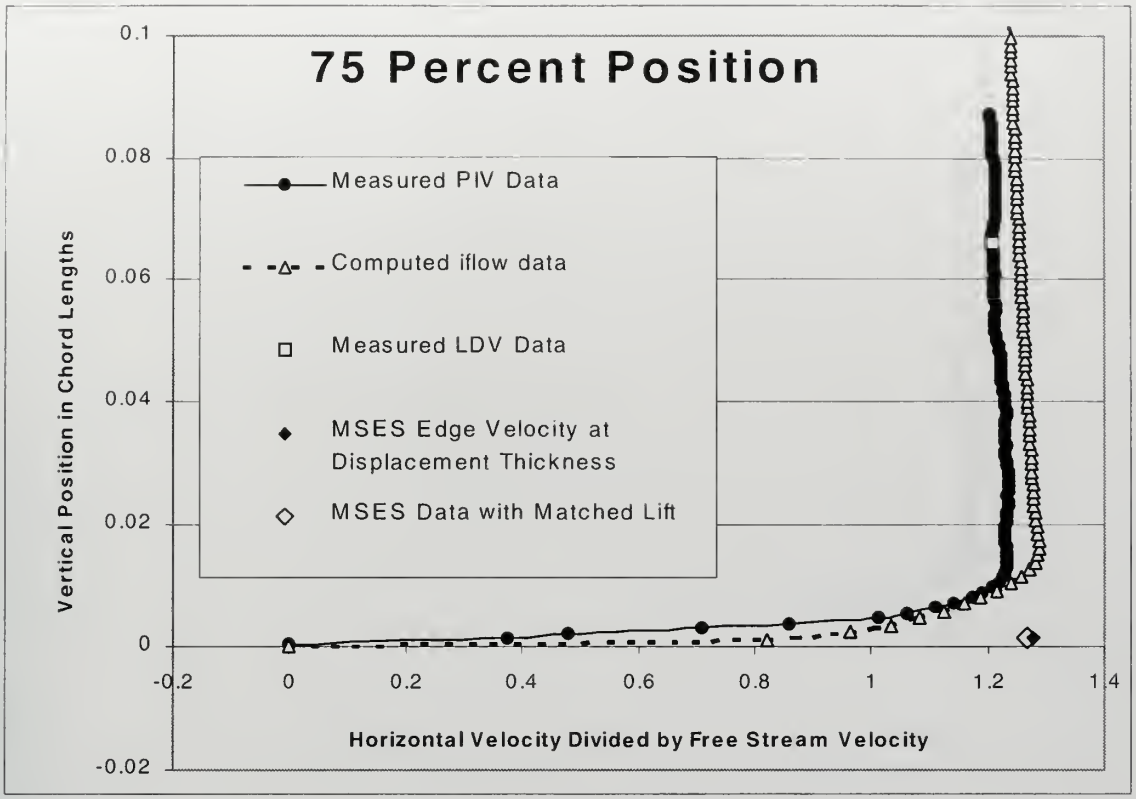
75 Percent Position
Measured PIV Data
Computed iflow data
Measured LDV Data
MSES Edge Velocity at Displacement Thickness
MSES Data with Matched Lift
Vertical Position in Chord Lengths
Horizontal Velocity Divided by Free Stream Velocity
0.1
0.08
0.06
0.04
0.02
0
-0.02
-0.2
0
0.2
0.4
0.6
0.8
1
1.2
1.4

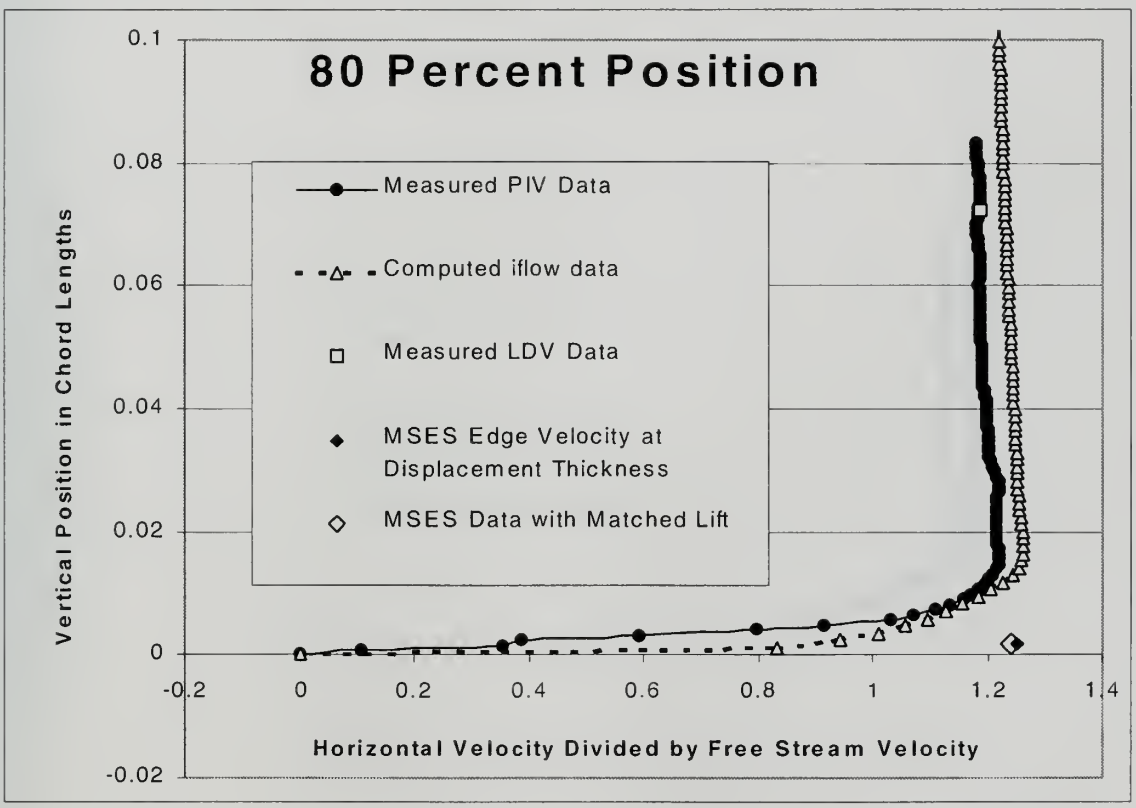
80 Percent Position
Measured PIV Data
Computed iflow data
Measured LDV Data
MSES Edge Velocity at Displacement Thickness
MSES Data with Matched Lift
Vertical Position in Chord Lengths
Horizontal Velocity Divided by Free Stream Velocity
0.1
0.08
0.06
0.04
0.02
0
-0.02
-0.2
0
0.2
0.4
0.6
0.8
1
1.2
1.4

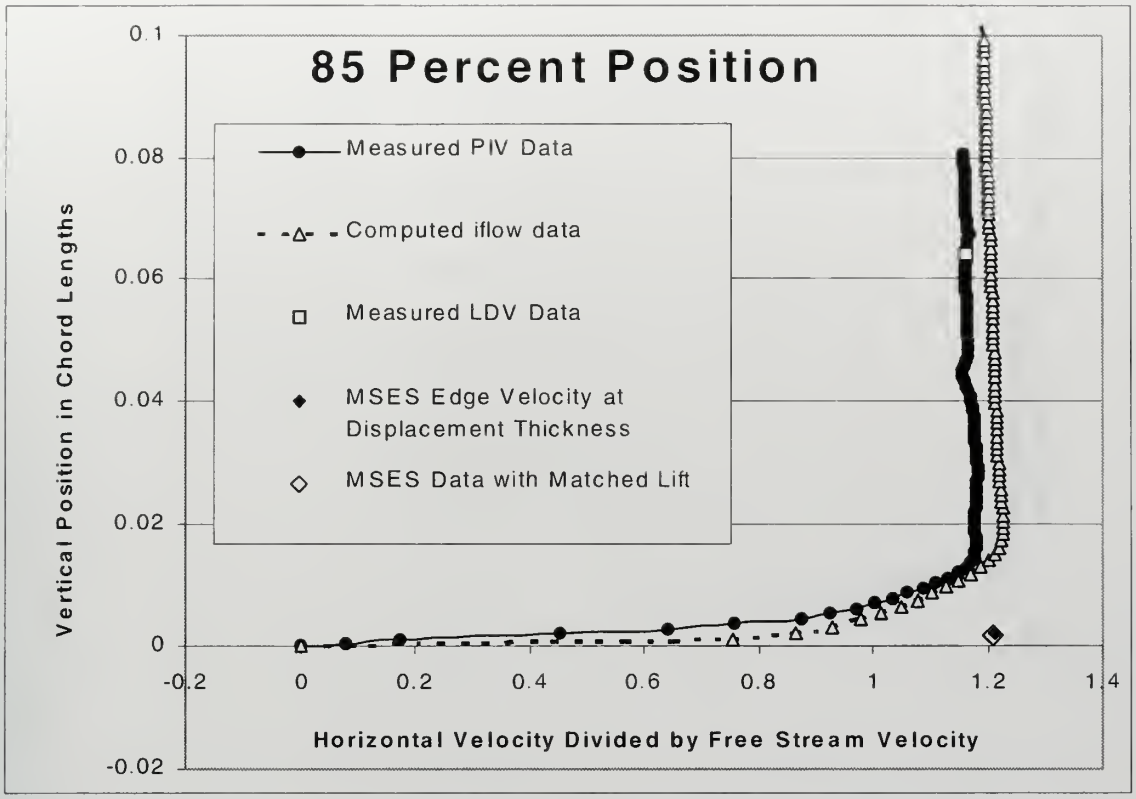
85 Percent Position
Measured PIV Data
Computed iflow data
Measured LDV Data
MSES Edge Velocity at Displacement Thickness
MSES Data with Matched Lift
Vertical Position in Chord Lengths
Horizontal Velocity Divided by Free Stream Velocity
0.1
0.08
0.06
0.04
0.02
0
-0.02
-0.2
0
0.2
0.4
0.6
0.8
1
1.2
1.4

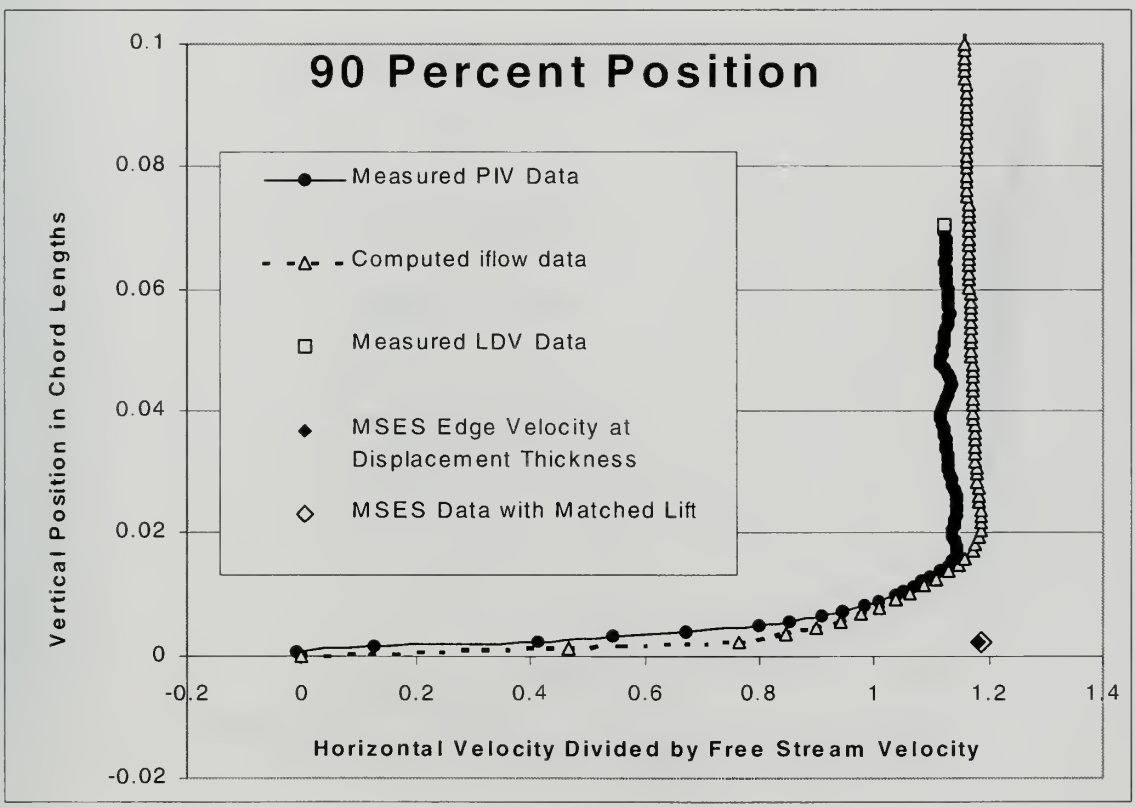
90 Percent Position
Measured PIV Data
Computed iflow data
Measured LDV Data
MSES Edge Velocity at Displacement Thickness
MSES Data with Matched Lift
Vertical Position in Chord Lengths
Horizontal Velocity Divided by Free Stream Velocity
0.1
0.08
0.06
0.04
0.02
0
-0.02
-0.2
0
0.2
0.4
0.6
0.8
1
1.2
1.4

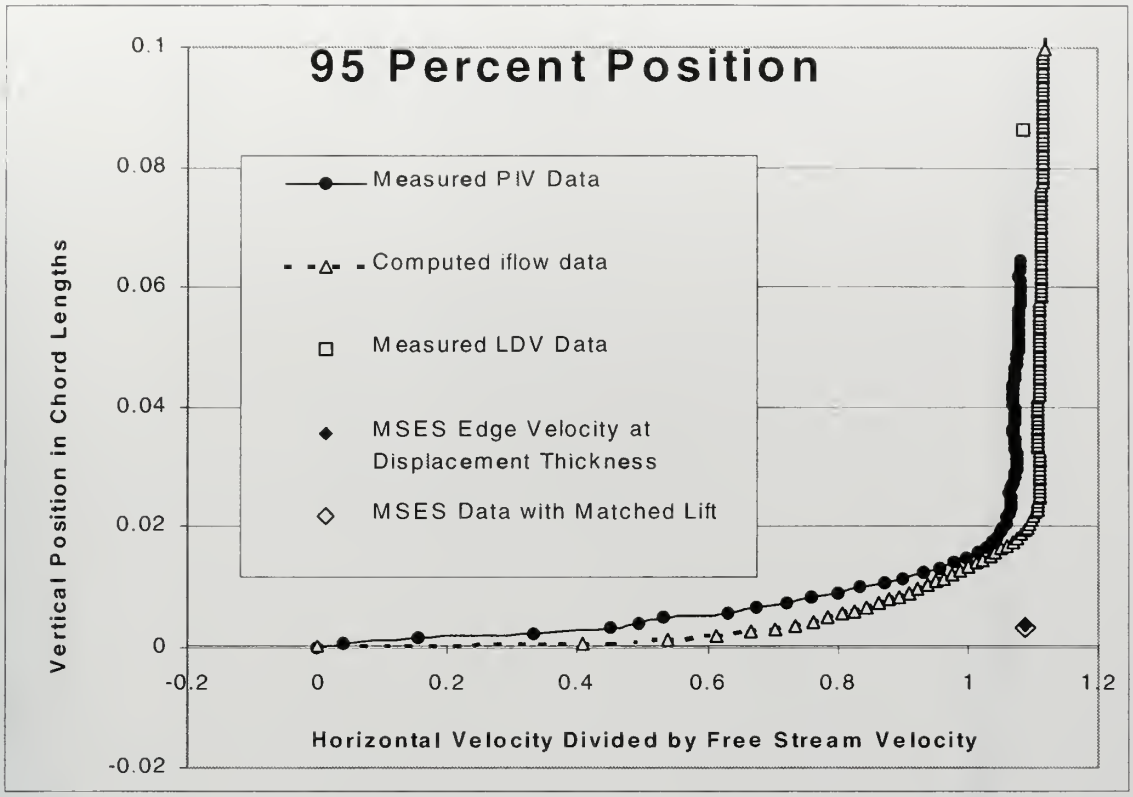
95 Percent Position
Measured PIV Data
Computed iflow data
Measured LDV Data
MSES Edge Velocity at Displacement Thickness
MSES Data with Matched Lift
Vertical Position in Chord Lengths
Horizontal Velocity Divided by Free Stream Velocity
0.1
0.08
0.06
0.04
0.02
0
-0.02
-0.2
0
0.2
0.4
0.6
0.8
1
1.2

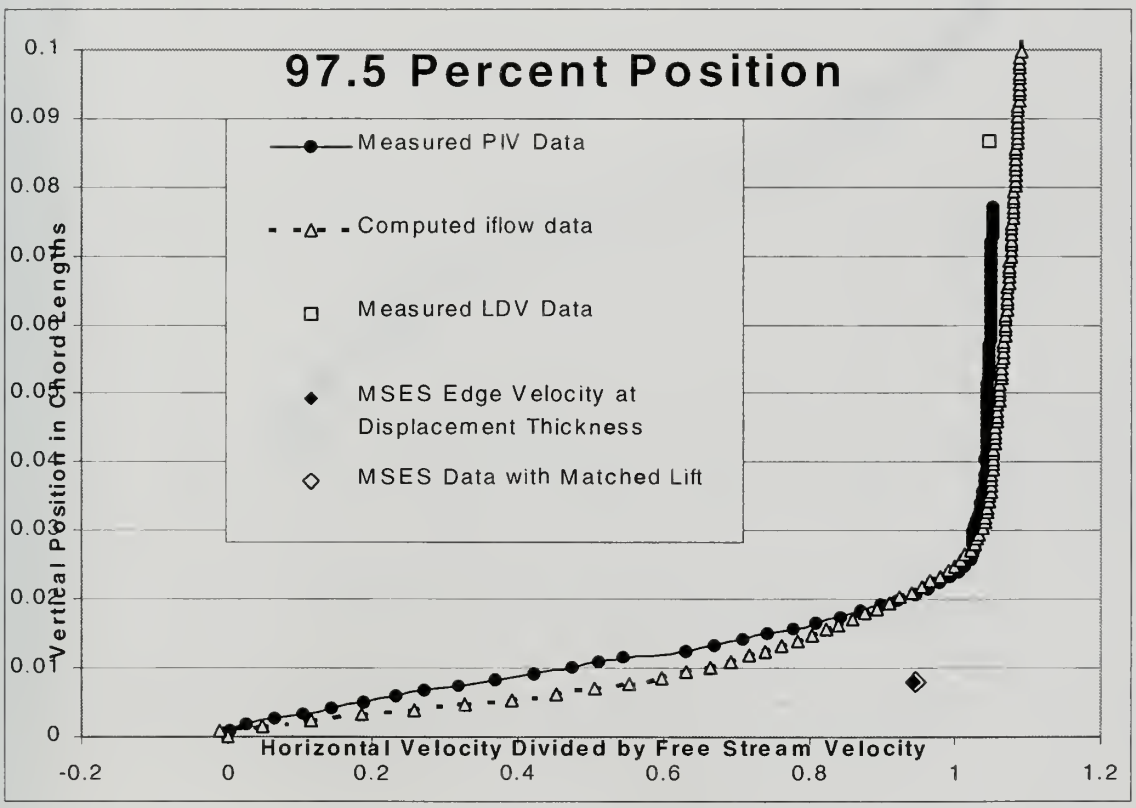
97.5 Percent Position
Measured PIV Data
Computed iflow data
Measured LDV Data
MSES Edge Velocity at Displacement Thickness
MSES Data with Matched Lift
Vertical Position in Chord Lengths
Horizontal Velocity Divided by Free Stream Velocity
0.1
0.09
0.08
0.07
0.06
0.05
0.04
0.03
0.02
0.01
0
-0.2
0
0.2
0.4
0.6
0.8
1
1.2

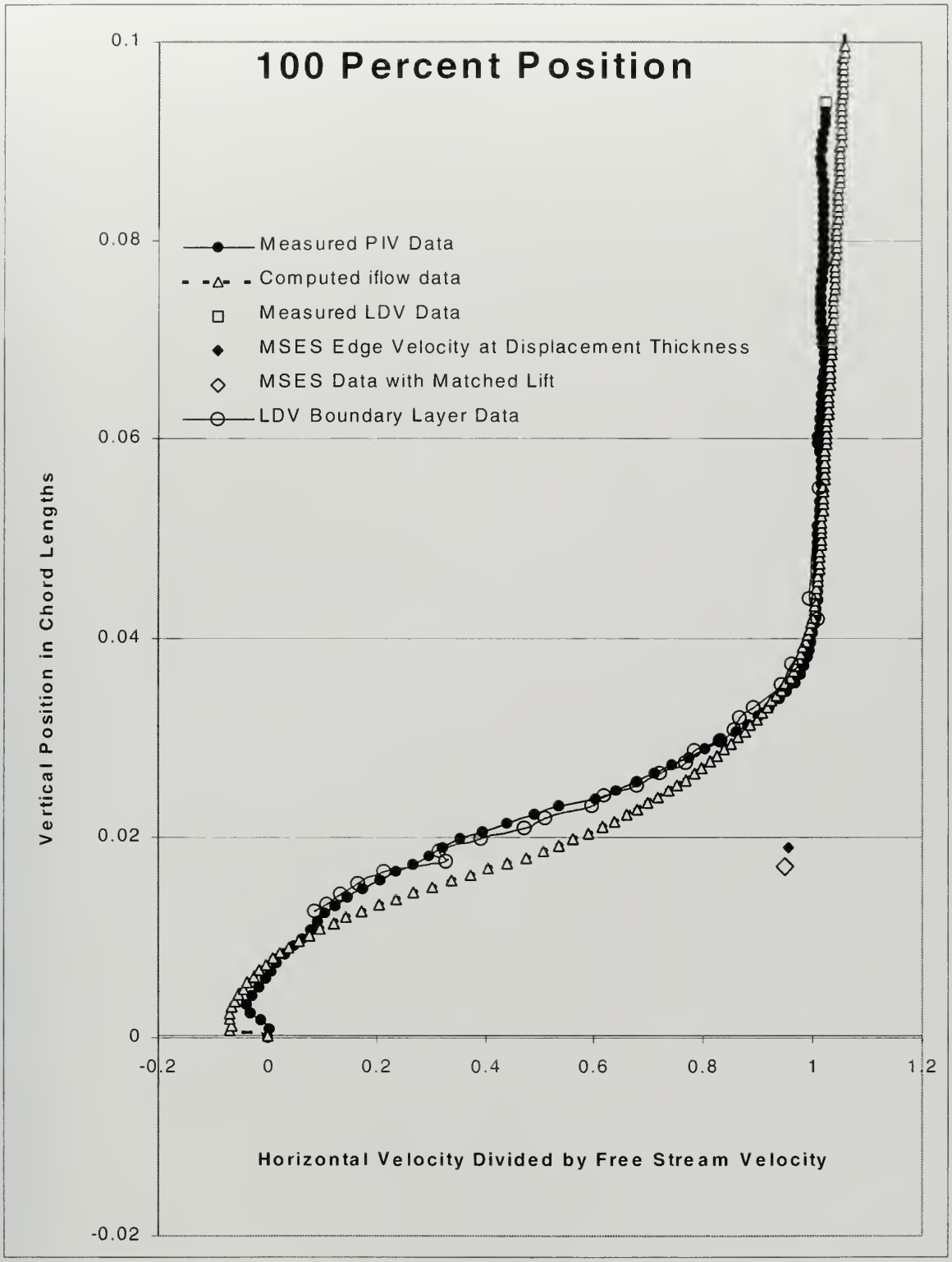
100 Percent Position
Measured PIV Data
Computed iflow data
Measured LDV Data
MSES Edge Velocity at Displacement Thickness
MSES Data with Matched Lift
LDV Boundary Layer Data
Vertical Position in Chord Lengths
Horizontal Velocity Divided by Free Stream Velocity
0.1
0.08
0.06
0.04
0.02
0
-0.02
-0.2
0
0.2
0.4
0.6
0.8
1
1.2